

# Cosmic-ray ionisation rate in low-mass cores: the role of the environment

E. Redaelli<sup>1,2</sup>, S. Bovino<sup>3,4,5</sup>, G. Sabatini<sup>3,6</sup>, D. Arzoumanian<sup>7,8,9</sup>, M. Padovani<sup>3</sup>, P. Caselli<sup>2</sup>, F. Wyrowski<sup>10</sup>, J. E. Pineda<sup>2</sup>, and G. Latrille<sup>5</sup>

<sup>1</sup> European Southern Observatory, Karl-Schwarzschild-Straße 2, 85748 Garching, Germany

<sup>2</sup> Max-Planck-Institut für Extraterrestrische Physik, Giessenbachstrasse 1, 85748 Garching, Germany

<sup>3</sup> INAF, Osservatorio Astrofisico di Arcetri, Largo E. Fermi 5, I-50125, Firenze, Italy

<sup>4</sup> Chemistry Department, Sapienza University of Rome, P.le A. Moro, 00185 Rome, Italy

<sup>5</sup> Departamento de Astronomía, Facultad Ciencias Físicas y Matemáticas, Universidad de Concepción, Av. Esteban Iturra s/n Barrio Universitario, Casilla 160, Concepción, Chile

<sup>6</sup> INAF, Istituto di Radioastronomia - Italian node of the ALMA Regional Centre (It-ARC), Via Gobetti 101, I-40129 Bologna, Italy

<sup>7</sup> Institute for Advanced Study, Kyushu University, Japan

<sup>8</sup> Department of Earth and Planetary Sciences, Faculty of Science, Kyushu University, Nishi-ku, Fukuoka 819-0395, Japan

<sup>9</sup> National Astronomical Observatory of Japan, 2-21-1 Osawa, Mitaka, Tokyo 181-8588, Japan

<sup>10</sup> Max-Planck-Institut für Radioastronomie, Auf dem Hügel, 69, 53121, Bonn, Germany

XXX

## ABSTRACT

**Context.** Cosmic rays drive several key processes for the chemistry and dynamical evolution of star-forming regions. Their effect is quantified mainly by means of the cosmic-ray ionisation rate  $\zeta_2$ .

**Aims.** We aim to obtain a sample of  $\zeta_2$  measurements in 20 low-mass starless cores embedded in different parental clouds, to assess the average level of ionisation in this kind of sources and to investigate the role of the environment in this context. The warmest clouds in our sample are Ophiuchus and Corona Australis, where star formation activity is higher than in the Taurus cloud and the other isolated cores we targeted.

**Methods.** We compute  $\zeta_2$  using an analytical method based on the column density of ortho- $\text{H}_2\text{D}^+$ , the CO abundance, and the deuteration level of  $\text{HCO}^+$ . To estimate these quantities, we analysed new, high-sensitivity molecular line observations obtained with the Atacama Pathfinder EXperiment (APEX) single-dish telescope and archival continuum data from *Herschel*.

**Results.** We report  $\zeta_2$  estimates in 17 cores in our sample and provide upper limits on the three remaining sources. The values span almost two orders of magnitude, from  $1.3 \times 10^{-18} \text{ s}^{-1}$  to  $8.5 \times 10^{-17} \text{ s}^{-1}$ .

**Conclusions.** We find no significant correlation between  $\zeta_2$  and the core's column densities  $N(\text{H}_2)$ . On the contrary, we find a positive correlation between  $\zeta_2$  and the cores' temperature, estimated via *Herschel* data: cores embedded in warmer environments present higher ionisation levels. The warmest clouds in our sample are Ophiuchus and Corona Australis, where star formation activity is higher than in the other clouds we targeted. The higher ionisation rates in these regions support the scenario that low-mass protostars in the vicinity of our targeted cores contribute to the re-acceleration of local cosmic rays.

**Key words.** ISM: cosmic rays – Star: formation – ISM: molecules – Astrochemistry – Molecular processes

## 1. Introduction

Cosmic rays (CRs) are energetic, ionised particles found ubiquitously in the interstellar medium (ISM). In the densest gas phases that represent the initial stage of star formation, the high visual extinction ( $A_V \gtrsim 6$  mag) is considered the threshold for star formation, cf. Froebrich & Rowles 2010; Pineda et al. 2023) completely attenuates the ultraviolet flux. In these conditions, without the existence of X-rays, CRs are the sole ionising agent. CRs ionise  $\text{H}_2$  molecules and produce  $\text{H}_3^+$ , which in turn determines the ionisation fraction within dense matter. This ionisation fraction plays a crucial role in regulating star formation by controlling the rate of ambipolar diffusion, a process that can slow down gravitational collapse (Mouschovias & Spitzer 1976).  $\text{H}_3^+$ , moreover, is a pivotal species for the chemical evolution of star-forming regions, because it drives the efficient ion chemistry. By reacting with deuterated hydrogen HD,  $\text{H}_3^+$  is converted into  $\text{H}_2\text{D}^+$ , which is the starting point of the deuteration process in

the cold molecular gas phase (see e.g. Ceccarelli et al. 2014a, and references therein). CRs deeply impact the chemistry and physics of the dense ISM (see Padovani et al. 2020, for a review on the topic).

Estimating the CR ionisation rate ( $\zeta_2$ , expressed relative to  $\text{H}_2$  molecules) from observations is still challenging. In the diffuse ISM ( $A_V \lesssim 1$  mag),  $\text{H}_3^+$  absorption lines against bright background OB stars can be directly used to infer  $\zeta_2$ . This is the approach followed for instance by McCall et al. (2003); Indriolo et al. (2007); Indriolo & McCall (2012), with typical results of the order of  $\zeta_2 \gtrsim 10^{-16} \text{ s}^{-1}$ . This method, however, relies on the estimate of the gas volume density  $n(\text{H}_2)$ . Traditionally, this parameter has been estimated by fitting the populations of excited rotational states of the molecule  $\text{C}_2$ , taking into account infrared pumping and collisional de-excitation (van Dishoeck & Black 1982). In a recent work, however, Obolentseva et al. (2024) re-evaluated  $\zeta_2$  towards 12 diffuse lines of sight, using 3D gas density distributions obtained from extinction maps (Eden-

hofer et al. 2024), which leads to lower  $n(\text{H}_2)$  values. As a result, the computed  $\zeta_2$  values are also lower by almost one order of magnitude. Incidentally, the new density estimates are in good agreement with the values obtained revising the available  $\text{C}_2$  data (Neufeld et al. 2024).

In the cold dense gas, a value of  $\zeta_2 \approx 1 - 3 \times 10^{-17} \text{ s}^{-1}$  is often assumed, for instance in chemical modelling or magneto-hydrodynamic simulations (cf. Sipilä et al. 2015; Kong et al. 2015; Bovino et al. 2019). Observational estimates, however, are spread over a wider range, depending also on the methodology used. At visual extinction higher than a few mag, the absorption lines of  $\text{H}_3^+$  cannot be detected anymore. Guelin et al. (1977, 1982) proposed an analytic expression to infer the ionisation fraction based on the kinetics of  $\text{DCO}^+$  and  $\text{HCO}^+$ , and Wootten et al. (1979) expanded the method to obtain constraints on  $\zeta_2$ . Caselli et al. (1998) later expanded the research, reporting the first large ( $\sim 20$  objects) sample of  $\zeta_2$  measurements in low-mass dense cores. Those authors used both an analytical method and a more detailed analysis using a chemical code. The analytical method, however, has been found to have strong limitations (see Caselli et al. 1998 itself; Caselli et al. 2002; more recently, Redaelli et al. 2024). Several other works tackled the problem of measuring  $\zeta_2$  at high densities, yielding to  $\zeta_2$  values scattered over a large range (Maret & Bergin 2007; Hezareh et al. 2008; Fuente et al. 2016; Redaelli et al. 2021b; Harju et al. 2024), typically from  $\sim 10^{-18} \text{ s}^{-1}$  to a few  $\times 10^{-16} \text{ s}^{-1}$ .

More recently, Bovino et al. (2020) proposed an analytical approach to determine  $\zeta_2$  in dense prestellar cores from the detection of  $\text{H}_2\text{D}^+$  (and, in particular, of its ortho spin state,  $\text{oH}_2\text{D}^+$ , which can be observed from the ground), starting from the formulation of Oka (2019). It is based on inferring the  $\text{H}_3^+$  abundance from that of its deuterated forms, using the deuterium fraction measured from  $\text{HCO}^+$  isotopologues. Redaelli et al. (2024), by applying the method on synthetic observations based on magneto-hydrodynamic simulations, found that it is usually accurate within a factor of 2 – 3. The method was applied in the high-mass regime by Sabatini et al. (2020) using observations made with the Atacama Pathfinder EXperiment 12-meter submillimeter telescope (APEX; Güsten et al. 2006) and the Institut de Radioastronomie Millimétrique (IRAM) 30m single-dish telescope. Their results present  $\zeta_2$  values in the range  $(0.7 - 6) \times 10^{-17} \text{ s}^{-1}$ , in agreement with theoretical predictions. Sabatini et al. (2023) used data from the Atacama Large Millimeter and sub-millimeter Array (ALMA), obtaining  $\zeta_2$  maps at high resolution in two high-mass clumps. Their findings are in agreement with the most recent predictions of cosmic-ray propagation and attenuation (Padovani et al. 2022). Socci et al. (2024) used the same method to estimate  $\zeta_2$  on parsec scales towards the Orion Molecular Clouds (OMC-2 and OMC-3) by combining IRAM-30m, *Herschel* and Planck observations. All these studies targeted high-mass star-forming regions, and no dedicated analysis based on the  $\text{oH}_2\text{D}^+$  methodology in the low-mass regime has been performed so far.

From the theoretical point of view, significant efforts have been made to constrain the  $\zeta_2$  in the ISM starting from models of CR propagation and attenuation, taking into account the continuous energy losses that they suffer when interacting with the gas. Padovani et al. (2009) computed the local CR spectrum using the continuous slowing-down approximation, and Padovani et al. (2018) further expanded the analysis to a higher column density regime. Padovani et al. (2022) introduced three main models for the relation between  $\zeta_2$  and the total gas column density  $N(\text{H}_2)$ , based on three distinct assumptions on the spectral slope  $\alpha$  of low-energy protons: model “low”  $\mathcal{L}$ , which uses  $\alpha = 0.1$ , re-

produces the most recent Voyager data (Cummings et al. 2016; Stone et al. 2019); model “high”  $\mathcal{H}$  adopts  $\alpha = -0.8$  and reproduces the high  $\zeta_2$  measured in the diffuse medium, and might not be needed anymore in light of the recent results of Obolentseva et al. (2024); the “up-most” model ( $\mathcal{U}$ ), with  $\alpha = -1.2$ , which can be considered an upper limit to the CR ionisation rate by Galactic CRs.

The use of different methods, based on distinct assumptions and observables, makes it hard to compare the observational results in a statistical way and to interpret them in the framework of current theoretical models. This work aims to produce a uniform sample of measurements of  $\zeta_2$  in 20 dense cores, in order to infer the typical  $\zeta_2$  value in starless/prestellar sources and to study potential environmental effects, such as proximity to CR sources. We use new high-sensitivity observations obtained with the APEX telescope and adopt the methodology of Bovino et al. (2020).

The paper is organised as follows. Section 2 describes the selection of the targets. Section 3 presents the observational data. The analysis is reported in Sect. 4. First, we describe how we infer the gas properties in terms of density and temperature from the available *Herschel* maps (Sect. 4.1); then we compute the column densities of the targeted molecular species (Sect. 4.2); in Sect. 4.3 we comment on the main sources of uncertainty in our methodology. Section 4.4 reports the estimates of the CO depletion factor and deuteration fraction, while Sect. 4.5 presents the results concerning  $\zeta_2$ . In Sect. 4.6 we assess the cores’ ionisation degree and dynamical states. We discuss the results in Sect. 5. A summary is presented in Sect. 6.

## 2. The source sample

The sample analysed in this work is constituted of 20 starless and/or prestellar cores embedded in nearby (distance  $\lesssim 250$  pc) low-mass star-forming regions. Table 1 lists their name, coordinates, and distances. To take advantage of observations already available, we included the six Ophiuchus cores from Bovino et al. (2021), who reported the detection of  $\text{oH}_2\text{D}^+(1_{1,0} - 1_{1,1})$  with APEX. We added the six objects belonging to the sample of Caselli et al. (2008) where  $\text{oH}_2\text{D}^+$  was detected using the Caltech Submillimeter Observatory (CSO): L1544 and TMC1-C in Taurus, Ophiuchus D in Ophiuchus, L183, L694-2, and L429.

To complete the target list, we extracted 8 sources from the sample of cores identified by the *Herschel* Gould Belt Survey (HGBS<sup>1</sup>; André et al. 2010. See Kirk et al. 2013; Marsh et al. 2016; Bresnahan et al. 2018 for the core catalogues). Caselli et al. (in prep.) selected a sample of 40 objects from these catalogues, chosen to have high central volume and column densities ( $n(\text{H}_2) > 10^5 \text{ cm}^{-3}$ ,  $N(\text{H}_2) > 5 \times 10^{22} \text{ cm}^{-2}$ ) and presented follow-up observations of high- $J$  transitions of  $\text{N}_2\text{H}^+$  and  $\text{N}_2\text{D}^+$ , obtained with APEX. Further publications focus on two specific cores (CrA 151, Redaelli et al. 2025; Oph 464, also known as IRAS16293E, Spezzano et al. 2025). We drew eight from this catalogue of starless sources in Corona Australis and Taurus. The seven cores in Ophiuchus also have correspondence to HGBS objects from Ladjelate et al. (2020), even though the coordinates of the centres are offset by  $5 - 20''$  when compared to our pointings (see Table 1 for more details).

After the observational campaign, we noted that the target CrA 050 contains a detected Class I Young Stellar Object (YSO)

<sup>1</sup> All data available at <http://gouldbelt-herschel.cea.fr/archives>.

**Table 1.** Properties of the sample targeted by this work. The gas column density and dust temperature are taken from the maps generated from the *Herschel* continuum data. The last column indicates the corresponding object in the HGBS catalogues (when present), and the distance offset to our pointing.

Core	Coordinates		Distance <sup>a</sup>	$N(\text{H}_2)^b$	$T_{\text{dust}}^b$	$L^c$	HGBS catalogue object
	R.A. (J2000)	Dec.(J2000)	pc	$10^{22} \text{ cm}^{-2}$	K	pc	
Taurus							
Tau 410	04 <sup>h</sup> 18 <sup>m</sup> 32.99 <sup>s</sup>	+28°28 <sup>m</sup> 29.0 <sup>s</sup>	130	1.8	11.4	0.096-0.149	Same
Tau 420	04 <sup>h</sup> 18 <sup>m</sup> 40.32 <sup>s</sup>	+28°23 <sup>m</sup> 16.0 <sup>s</sup>	130	4.0	12.8	0.064-0.120	Same
TMC1-C <sup>d</sup>	04 <sup>h</sup> 41 <sup>m</sup> 34.31 <sup>s</sup>	+26°00 <sup>m</sup> 40.0 <sup>s</sup>	140	1.9	11.3	0.129-0.157	-
L1544	05 <sup>h</sup> 04 <sup>m</sup> 17.21 <sup>s</sup>	+25°10 <sup>m</sup> 42.8 <sup>s</sup>	170	11.6	10.2	0.073-0.125	-
Isolated cores							
L183	15 <sup>h</sup> 54 <sup>m</sup> 08.56 <sup>s</sup>	-02°52 <sup>m</sup> 49.0 <sup>s</sup>	110	5.9	9.6	0.052-0.077	-
L429	18 <sup>h</sup> 17 <sup>m</sup> 05.53 <sup>s</sup>	-08°13 <sup>m</sup> 29.9 <sup>s</sup>	200	5.1	9.9	0.065-0.109	-
L694-2	19 <sup>h</sup> 41 <sup>m</sup> 05.03 <sup>s</sup>	+10°57 <sup>m</sup> 02.0 <sup>s</sup>	250	4.3	9.8	0.077-0.111	-
Ophiuchus							
Oph 1	16 <sup>h</sup> 31 <sup>m</sup> 57.63 <sup>s</sup>	-24°57 <sup>m</sup> 35.7 <sup>s</sup>	140	3.8	13.4	0.067-0.141	Oph 410+412 <sup>e</sup>
Oph 2	16 <sup>h</sup> 31 <sup>m</sup> 39.94 <sup>s</sup>	-24°49 <sup>m</sup> 50.3 <sup>s</sup>	140	5.2	13.3	0.075-0.115	Oph 387 (24'')
Oph 3	16 <sup>h</sup> 27 <sup>m</sup> 33.24 <sup>s</sup>	-24°26 <sup>m</sup> 24.1 <sup>s</sup>	140	7.8	12.5	0.085-0.110	Oph 246 (7.8'')
Oph 4	16 <sup>h</sup> 27 <sup>m</sup> 12.77 <sup>s</sup>	-24°29 <sup>m</sup> 40.3 <sup>s</sup>	140	5.6	13.9	0.084-0.142	Oph 196 (9.2'')
Oph 5	16 <sup>h</sup> 27 <sup>m</sup> 15.28 <sup>s</sup>	-24°30 <sup>m</sup> 30.1 <sup>s</sup>	140	5.4	13.9	0.081-0.125	Oph 201 (11'')
Oph 6	16 <sup>h</sup> 27 <sup>m</sup> 19.99 <sup>s</sup>	-24°27 <sup>m</sup> 17.6 <sup>s</sup>	140	4.7	13.8	0.117-0.155	Oph 215 (5.7'')
Oph D	16 <sup>h</sup> 28 <sup>m</sup> 28.56 <sup>s</sup>	-24°19 <sup>m</sup> 25.0 <sup>s</sup>	140	1.7	13.3	0.076-0.108	Oph 316 (11'')
Corona Australis							
CrA 038	19 <sup>h</sup> 01 <sup>m</sup> 46.10 <sup>s</sup>	-36°55 <sup>m</sup> 35.7 <sup>s</sup>	150	6.2	13.7	0.078-0.109	Same
CrA 040	19 <sup>h</sup> 01 <sup>m</sup> 47.28 <sup>s</sup>	-36°56 <sup>m</sup> 39.8 <sup>s</sup>	150	4.6	15.5	0.115-0.144	Same
CrA 044	19 <sup>h</sup> 01 <sup>m</sup> 54.45 <sup>s</sup>	-36°57 <sup>m</sup> 48.9 <sup>s</sup>	150	10.5	18.2	0.044-0.074	Same
CrA 047	19 <sup>h</sup> 01 <sup>m</sup> 55.86 <sup>s</sup>	-36°57 <sup>m</sup> 46.9 <sup>s</sup>	150	9.9	19.0	0.044-0.071	Same
CrA 050 <sup>f</sup>	19 <sup>h</sup> 01 <sup>m</sup> 58.94 <sup>s</sup>	-36°57 <sup>m</sup> 09.9 <sup>s</sup>	150	3.5	18.0	0.107-0.132	Same
CrA 151	19 <sup>h</sup> 10 <sup>m</sup> 20.17 <sup>s</sup>	-37°08 <sup>m</sup> 27.0 <sup>s</sup>	150	4.1	11.2	0.041-0.076	Same

**Notes.** <sup>(a)</sup> Distance references: Ophiuchus, Ortiz-León et al. (2018); Taurus, Galli et al. (2019); Corona Australis, Galli et al. (2020); L183, L429, L694-2, Redaelli et al. (2018, and references therein).

<sup>(b)</sup> Values towards the cores' coordinates, averaged in a 37'' beam.

<sup>(c)</sup> Path length along the line-of-sight from where the molecular emission arises in Eq. 1. The two values correspond to the equivalent diameter of the region encompassing the 60% and 40% contours of the  $N(\text{H}_2)$  peak value, as described in Sect. 4.5.

<sup>(d)</sup> The TMC1-C pointing is offset by  $\approx 60''$  compared to the one of Caselli et al. (2008).

<sup>(e)</sup> Oph 1 is found roughly halfway between the centres of Oph 410 (22'' to the North-West) and Oph 412 (18'' to the South-West) from the HGBS catalogue. For the DCO<sup>+</sup> (4-3) spectrum towards this object, we have taken the average of the two spectra. Their intensities differ by  $\sim 5\%$ .

<sup>(f)</sup> CrA 050 contains a detected YSO within its boundaries (source SMM2, Sicilia-Aguilar et al. 2013). This is a young, Class I object.

within the core boundaries (Sicilia-Aguilar et al. 2013). We decided to keep the core in the sample, however, to investigate the ionisation rate in a young protostellar envelope. Furthermore, Redaelli et al. (2025) discussed that CrA 151 might also contain a very young protostar, but the evidence is so far inconclusive.

### 3. Observations

#### 3.1. APEX data

The molecular line observations were performed with the APEX single-dish antenna as part of two projects, IDs M9505A\_111 and M9503A\_112 (PI: E. Redaelli). In March and June 2023, we observed the sources in Ophiuchus, Corona, and the isolated ones (L429, L694-2, L183). The Taurus cores were instead observed in the second half of 2023.

We used four spectral setups in total. Setup 1 covered the oH<sub>2</sub>D<sup>+</sup>(1<sub>1,0</sub> – 1<sub>1,1</sub>) using the LAsMA receiver (Güsten et al.

2008), and it was not re-observed in the six Ophiuchus cores of Bovino et al. (2021). Setup 2 covered simultaneously the DCO<sup>+</sup> (3-2) and C<sup>18</sup>O (2-1) lines using the receiver nFLASH230. Setup 3 was dedicated to the HC<sup>18</sup>O<sup>+</sup> and H<sup>13</sup>CO<sup>+</sup> (2-1) lines using the receiver SEPIA180 (Belitsky et al. 2018a,b). Setup 4 covered simultaneously the HCO<sup>+</sup> and H<sup>13</sup>CO<sup>+</sup> (3-2) lines using nFLASH230.

For all the setups, we used the APEX FFTS spectrometer at the highest resolution of 64 kHz, which translates into a velocity resolution of 0.05 – 0.11 km s<sup>-1</sup>. The observations were performed as single-pointings towards the cores' coordinates listed in Table 1 (see also Fig. 1). In the case of LAsMA, a multi-beam receiver, we set the central beam in the core centre. The only exception is Ophiuchus D, where instead the core centre was located in one of the six external beams, to ensure the same spatial coverage as previous observations. We used the position switching observation mode, with the off-position hand-picked usually 0.5° away from the on position.

In addition, we analysed the published  $\text{oH}_2\text{D}^+(1_{1,0} - 1_{1,1})$  data towards the cores Oph 1 - Oph 6. We refer to Bovino et al. (2021) for an exhaustive description of the observations. We also used  $\text{DCO}^+$  (4-3) observations obtained with APEX, which are available for all the targets except L429, L183, L694-2, TMC1-C, and L1544 (from Caselli et al., in prep.).

We reduced the data using the `CLASS` package from the `GILDAS` software<sup>2</sup> (Pety 2005). In particular, we subtracted baselines (usually a first-order polynomial) in every single scan, and then averaged them. The intensity scale was converted in main beam temperature  $T_{\text{MB}}$  assuming the forward efficiency  $F_{\text{eff}} = 0.95$  and computing the main-beam efficiency  $\eta_{\text{MB}}$  at each frequency based on the data tabulated at <https://www.apex-telescope.org/telescope/efficiency/index.php>. Relevant information on the targeted transitions and their observational parameters is given in Table 2, including the angular resolution ( $\theta_{\text{MB}}$ ) of the observations, the main-beam efficiency values, and the velocity resolution  $\Delta V_{\text{ch}}$ .

### 3.2. Continuum data

The methodology we applied (see Sect. 4) requires knowledge of the gas total column density and temperature. We have used available maps of  $N(\text{H}_2)$  and dust temperature  $T_{\text{dust}}$  derived from the spectral-energy-distribution (SED) fit of the dust continuum emission detected with *Herschel*. In particular, for the cores in Ophiuchus, Corona Australis, and Taurus (except for L1544) we have used the maps provided by the HGBS survey<sup>3</sup>. For the remaining cores, we have used the maps published in Spezzano et al. (2017, for L1544) and Redaelli et al. (2018, for L429, L694-2, and L183). The HGBS survey provides  $\text{H}_2$  column density map at the high angular resolution of  $18.2''$  (cf. Palmeirim et al. 2013). In this work, however, we used the products at the larger angular resolution of the SPIRE/500  $\mu\text{m}$  wavelength ( $\approx 37''$ ). This is closer to the APEX resolution at  $\sim 2$  mm, and it is the one available for L183, L429, L694-2, and L1544.

## 4. Analysis and Results

To compute  $\zeta_2$ , we applied the analytical formula of Bovino et al. (2020), which was derived from first principles and has the advantage of being model-independent. We refer to that paper and to Redaelli et al. (2024) for a complete description of the method assumptions and limitations. The approach is based on the detection of the first deuterated form of  $\text{H}_3^+$ , i.e.  $\text{oH}_2\text{D}^+$ :

$$\zeta_2 = k_{\text{CO}}^{\text{oH}_3^+} \frac{1}{3} \times X(\text{CO}) \times \frac{N(\text{oH}_2\text{D}^+)}{R_{\text{D}}} \frac{1}{L}, \quad (1)$$

where the deuterium fraction of  $\text{HCO}^+$  is  $R_{\text{D}} = N(\text{DCO}^+)/N(\text{HCO}^+)$ , the CO abundance (with respect to  $\text{H}_2$ ) is  $X(\text{CO}) = N(\text{CO})/N(\text{H}_2)$ , and  $N(\text{oH}_2\text{D}^+)$  is the column density of  $\text{oH}_2\text{D}^+$ .  $k_{\text{CO}}^{\text{oH}_3^+}$  is the destruction rate of  $\text{oH}_3^+$  by CO, assumed here to be the main destruction path for  $\text{H}_3^+$ , while  $L$  is the path length over which the column densities are estimated. The  $k_{\text{CO}}^{\text{oH}_3^+}$  rate is temperature dependent, and we have computed it in each core assuming  $T_{\text{gas}} = T_{\text{dust}}$ , hence assuming dust and gas coupling (expected to be efficient at  $n \gtrsim 10^{4-5} \text{ cm}^{-3}$ , Goldsmith 2001). Sokolov et al. (2017) showed that the difference in

the two temperatures can be of the order of 2 K, supporting that this is a good approximation. The rate value is taken from the KIDA<sup>4</sup> database (Wakelam et al. 2012), and it presents a modest decrease in the temperature range 8 – 20 K.

We used the optically thinner  $\text{C}^{18}\text{O}$  to infer the CO abundance, assuming  $X(\text{CO}) = 557 \times X(\text{C}^{18}\text{O})$  (Wilson 1999), avoiding opacity issues. For the same reason, the  $\text{HCO}^+$  deuteration level has been computed from  $\text{DCO}^+$  and the rarer  $\text{H}^{13}\text{CO}^+$  isotopologue, assuming the isotopic ratio of  $^{12}\text{C}/^{13}\text{C} = 68$  (Wilson 1999). In fact, the  $\text{HCO}^+$  (3-2) transition presents in most sources double-peak profiles with asymmetries, indicative of self-absorption, and it is not suitable to infer the molecular abundance. The  $\text{HC}^{18}\text{O}^+$  (2-1) is detected only in 60% of the sample, and we do not include it in the analysis. However, we use it later to check the carbon isotopic ratio in the sample (see Sect. 4.3).

### 4.1. Total gas column density and dust temperature

To assign to each core a value of total gas column density  $N(\text{H}_2)$  and dust temperature  $T_{\text{dust}}$ , we have taken the maps listed in Sect. 3.2. We cut square regions of  $4' \times 4'$  around the cores' central coordinates. The maps are shown in Fig. 1. We measured the average  $T_{\text{dust}}$  and  $N(\text{H}_2)$  in one *Herschel* beam ( $37''$ ) around the centre. The values are listed in Table 1.

The cores span the temperature range of 9 – 20 K, with a mean value of 13 K. The warmest sources all belong to the Corona Australis region (CrA 038, 040, 044, 047, and 050), in particular in the area of the Coronet cluster, a well-known active star-forming region (cf. Chini et al. 2003; Sicilia-Aguilar et al. 2013; Sabatini et al. 2024). The column density values range from a minimum of  $1.7 \times 10^{22} \text{ cm}^{-2}$  (Oph D), to a maximum of  $1.16 \times 10^{23} \text{ cm}^{-2}$  (L1544), i.e. approximately one order of magnitude of variation.

### 4.2. Molecular column densities

The estimate of  $\zeta_2$  depends on the measurements of column densities of four distinct tracers in Eq. (1). We adopted the constant excitation temperature approach (C-TEX, Caselli et al. 2002) to fit the observed spectra and derive the column density ( $N_{\text{col}}$ ) for each species. The fitting procedure is implemented using the `PYTHON` package `PYSPECKIT` (Ginsburg & Mirocha 2011; Ginsburg et al. 2022), with the spectroscopic constants listed in Table 2. The partition function of  $\text{DCO}^+$  is taken from Redaelli et al. (2019), of  $\text{C}^{18}\text{O}$ ,  $\text{HCO}^+$ ,  $\text{H}^{13}\text{CO}^+$ , and  $\text{HC}^{18}\text{O}^+$  from the CDMS database, and of  $\text{oH}_2\text{D}^+$  from our own calculation based on the energy data provided by CDMS<sup>5</sup>. We highlight that the transitions from D-bearing species ( $\text{DCO}^+$ ,  $\text{oH}_2\text{D}^+$ ) present hyperfine splitting due to the nuclear spin of the deuterium atom. However, the hyperfine structure is usually unresolved given the spectral resolution of our observations (cf. Caselli & Dore 2005). Since we are not interested in high-precision kinematic measurements in this work (where including the hyperfine structure would be relevant), we neglect it.

The code fits the observed spectra using four free parameters: the line centroid velocity  $V_{\text{lsr}}$ , the line velocity dispersion  $\sigma_v$ , the molecular column density  $N_{\text{col}}$  and the excitation temperature  $T_{\text{ex}}$ . When two transitions from the same species are available, the method assumes that  $T_{\text{ex}}$  is equal for all transitions.

<sup>4</sup> <https://kida.astrochem-tools.org>.

<sup>5</sup> The partition function of  $\text{oH}_2\text{D}^+$  at the temperature  $T$  is computed using  $Q = \sum_i g_{u,i} \exp\left(-\frac{E_{u,i}}{k_B T}\right)$ , where  $g_{u,i}$  and  $E_{u,i}$  are the degeneracy and energy of the upper  $i$  level.

<sup>2</sup> Available at <http://www.iram.fr/IRAMFR/GILDAS/>.

<sup>3</sup> The detailed references are: Bresnahan et al. (2018) for Corona; Roy et al. (2014) and Ladjelate et al. (2020) for Ophiuchus; Palmeirim et al. (2013) for Taurus.

**Table 2.** Properties of the targeted lines. We list the frequency ( $\nu$ ), angular resolution, main-beam efficiency, and velocity resolution. In the last three columns, we report the spectroscopic constants used in the column density computation (see Sect. 4.2). They are taken from the CDMS catalogue (Müller et al. 2005).

Transition	$\nu$ MHz	$\theta_{\text{MB}}$ "	$\eta_{\text{MB}}$	$\Delta V_{\text{ch}}$ km s <sup>-1</sup>	$A_{\text{ul}}$ $\times 10^{-5} \text{ s}^{-1}$	$g_{\text{u}}$	$E_{\text{u}}$ K
HC <sup>18</sup> O <sup>+</sup> (2-1)	170322.626	35.4	0.86	0.11	34.99	5	12.26
H <sup>13</sup> CO <sup>+</sup> (2-1)	173506.700	34.7	0.86	0.11	36.99	5	12.49
DCO <sup>+</sup> (3-2)	216112.582	27.9	0.82	0.08	76.58	7	12.49
C <sup>18</sup> O (2-1)	219560.350	27.5	0.82	0.08	0.0601	5	15.80
H <sup>13</sup> CO <sup>+</sup> (3-2)	260255.339	23.2	0.78	0.07	133.75	7	24.98
HCO <sup>+</sup> (3-2)	267557.626	22.5	0.78	0.07	145.30	7	25.68
DCO <sup>+</sup> (4-3)	288143.858	20.9	0.76	0.06	188.23	9	34.57
oH <sub>2</sub> D <sup>+</sup> (1 <sub>1,0</sub> – 1 <sub>1,1</sub> )	372421.356	16.2	0.69	0.05 <sup>a</sup>	10.96	9	17.90

**Notes.** <sup>(a)</sup> The velocity resolution of the archival APEX data for oH<sub>2</sub>D<sup>+</sup>(1<sub>1,0</sub> – 1<sub>1,1</sub>) in cores Oph 1-6 is 0.2 km s<sup>-1</sup> (Bovino et al. 2021).

This allows fitting  $T_{\text{ex}}$  and  $N_{\text{col}}$  simultaneously. We estimated the column density of H<sup>13</sup>CO<sup>+</sup> with this approach in the whole sample, except for L1544, Tau 410, and TMC1-C, where H<sup>13</sup>CO<sup>+</sup> (3-2) is not detected<sup>6</sup>. Similarly, the (3-2) and (4-3) transitions of DCO<sup>+</sup> are available for 14 out of 20 targets.

In Fig. 2 we compare the  $T_{\text{ex}}$  values obtained for DCO<sup>+</sup> and H<sup>13</sup>CO<sup>+</sup> in all the cores where this has been possible, also with the  $T_{\text{dust}}$  values obtained as described in Sect. 4.1. In general, the excitation temperatures are lower than the corresponding  $T_{\text{dust}}$  value by 6% for DCO<sup>+</sup> and by 34% for H<sup>13</sup>CO<sup>+</sup>. This indicates that the lines are generally sub-thermally excited, i.e. the collisional excitations are not efficient enough to counterbalance the radiative de-excitations, or that the  $T_{\text{dust}}$  is overestimating the gas temperature, because of line-of-sight averaging (see Sokolov et al. 2017). The first effect is expected as these lines have high critical densities, which can be higher than the average densities of the cores. Interestingly, the DCO<sup>+</sup>  $T_{\text{ex}}$  is on average higher than the H<sup>13</sup>CO<sup>+</sup> one: considering all cases where we have estimates for both,  $T_{\text{ex}}(\text{DCO}^+) = 1.4 \times T_{\text{ex}}(\text{H}^{13}\text{CO}^+)$ . We struggle to find an explanation for this behaviour. The fact that the former is estimated using higher- $J$  transitions than the latter (hence with higher critical densities) should point in the opposite direction. Furthermore, H<sup>13</sup>CO<sup>+</sup> is not systematically less abundant than DCO<sup>+</sup>, which could justify a difference in excitation conditions. The average optical depth of these lines is consistently  $\tau < 1$ , which rules out opacity issues (see Table A.1). Figure A.19 shows the comparison of the centroid velocity and velocity dispersion values in the whole sample. The  $V_{\text{lsr}}$  values are remarkably consistent within each other. The  $\sigma_{\text{v}}$  values present a higher scatter, and in 68% of sources the DCO<sup>+</sup> lines are narrower than the H<sup>13</sup>CO<sup>+</sup> ones. A possible explanation is that the H<sup>13</sup>CO<sup>+</sup> lines are tracing slightly lower densities than the DCO<sup>+</sup> lines, as *i*) deuteration is expected to increase towards the centre and *ii*) the angular resolution of H<sup>13</sup>CO<sup>+</sup> data is worse than the DCO<sup>+</sup> one, which could cause more lower density material to be intercepted by the H<sup>13</sup>CO<sup>+</sup> emission.

For the species with one detected line,  $T_{\text{ex}}$  and  $N_{\text{col}}$  are degenerate parameters, and the former must be assumed to estimate the latter. We highlight that this choice is arbitrary, as there is no general prescription to estimate  $T_{\text{ex}}$ . We proceed as follows. For H<sup>13</sup>CO<sup>+</sup> and DCO<sup>+</sup>, in those cases where only one line is detected or available, we compute  $T_{\text{ex}}$  based on the  $T_{\text{dust}}$  val-

ues, using the corrective factors computed above (0.94 for DCO<sup>+</sup> and 0.66 for H<sup>13</sup>CO<sup>+</sup>). For oH<sub>2</sub>D<sup>+</sup> we adopt the same  $T_{\text{ex}}$  as of DCO<sup>+</sup>. These values are in the range 6 – 22 K and they compare well with previous studies of the same molecule (Vastel et al. 2006; Caselli et al. 2008; Redaelli et al. 2021a, 2022). For C<sup>18</sup>O we assume  $T_{\text{dust}} = T_{\text{ex}}$ , because this is an abundant species with low critical density and it is likely to be thermalised.

Figure 3 showcases an example of the best-fit solutions found towards CrA 151. The lines are well reproduced by the spectral modelling. For a few sources in the sample, however, the line profiles deviate from single Gaussian components. This is the case, for instance, for Oph 4, shown in Fig. 4, where two clear velocity components (one at  $\sim 3.4 \text{ km s}^{-1}$  and one at  $\sim 3.9 \text{ km s}^{-1}$ ) are visible. For the cases where two velocity components can be seen in all transitions, we perform the fit routine previously described with two components, deriving two sets of molecular column densities for the same target. We then sum the two contributions to obtain one column density value for each species in each core. This is necessary, as the  $T_{\text{dust}}$  and total column density values obtained from the continuum maps cannot distinguish among distinct velocity components. This approach is used for Oph 3 and Oph 4. For other cores where the multiple components are not visible in all tracers or they are too overlapped for the fit to converge, we adopt the single-component procedure, in line with our goal to infer an average  $\zeta_2$  value across each core. Table 3 summarises the  $T_{\text{ex}}$  and  $N_{\text{col}}$  values obtained as just described. The complete set of figures for all cores is available in Appendix A. Table A.1 lists the derived best-fit values for the remaining free parameters, line velocity dispersion and centroid velocity.

#### 4.3. Uncertainties in the column density estimations

We made several assumptions in the methodology to compute column densities described in Sect. 4.2. Here, we discuss the main ones.

##### 4.3.1. Optical depths

In this work we used H<sup>13</sup>CO<sup>+</sup> and C<sup>18</sup>O to trace the total abundance of the corresponding main isotopologues, in the assumption that they are optically thin. To verify this point, the fitting routine implemented in PYSPECKIT returns the peak optical depth  $\tau$  of each transition. We computed the mean and standard de-

<sup>6</sup> In L1544, a tentative detection of H<sup>13</sup>CO<sup>+</sup> (3-2) was found, but the low S/N ( $\sim 3$ ) prevents the fit from converging.

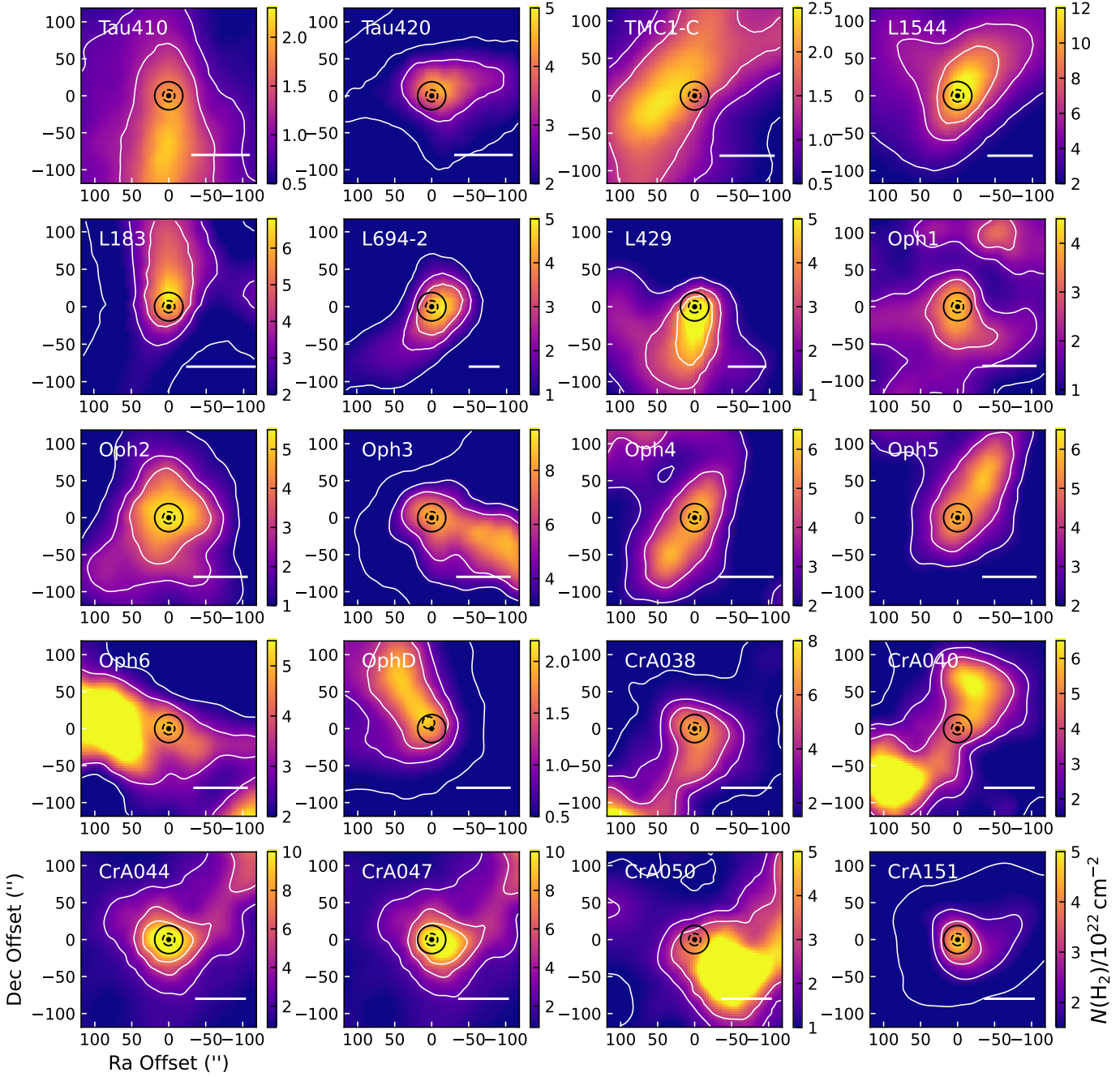


**Fig. 1.**  $N(\text{H}_2)$  maps towards each core in the sample (labelled in the top-left corner of every panel). The scalebar shown in the bottom-right corner represents a length of 0.05 pc. The white contours show the 20, 40, and 60% levels of the peak value within the central *Herschel* beam. The solid circles show the APEX pointing and the  $N(\text{H}_2)$  map beam size, whilst the dashed circles show the beam sizes and pointings of APEX for the  $\text{oH}_2\text{D}^+$  line. Note the small shift present between the two positions for Oph D, where the  $\text{oH}_2\text{D}^+$  beam is not the central LAsMA beam, but one of the external ones (see Main Text). The shift is however smaller than the continuum and APEX resolutions.

violation of the  $\tau$  distributions, obtaining:  $\tau(\text{H}^{13}\text{CO}^+ 2-1) = 0.44 \pm 0.26$ ,  $\tau(\text{H}^{13}\text{CO}^+ 3-2) = 0.26 \pm 0.12$ , and  $\tau(\text{C}^{18}\text{O } 2-1) = 0.73 \pm 0.23$ . All these values are consistently lower than 1.0, indicating general optically-thin conditions.

For completeness, we report also the values for the remaining lines:  $\tau(\text{DCO}^+ 3-2) = 0.58 \pm 0.99$ ,  $\tau(\text{DCO}^+ 4-3) = 0.30 \pm 0.27$ , and  $\tau(\text{oH}_2\text{D}^+ 1_{1,0} - 1_{1,1}) = 0.22 \pm 0.20$ . The mean values are  $< 1.0$ . All the transitions are on average optically thin across the sample. The optical depth values in the whole sample are available in Table A.1.

#### 4.3.2. Isotopic ratios

When using rarer isotopologues, we assumed the isotopic ratios  $^{16}\text{O}/^{18}\text{O} = 557$  and  $^{12}\text{C}/^{13}\text{C} = 68$  to infer the total column densities of the main species. However, recent chemical modelling work showed that carbon fractionation may lead to significant variations (up to a factor of 2) of the  $^{12}\text{C}/^{13}\text{C}$  ratio (Colzi et al. 2020; Loison et al. 2020). The expected variations of the oxygen isotopic ratio are more modest (Loison et al. 2019). For 12 targets in our sample, we have detected the  $\text{HC}^{18}\text{O}^+ (2-1)$  line. We have, hence, compared the flux ratio of the  $\text{H}^{13}\text{CO}^+$

**Table 3.** Molecular excitation temperatures and column densities obtained by fitting the observed spectral lines. When the  $T_{\text{ex}}$  value is presented without uncertainties, its value has been assumed and fixed in the fit (see the Main Text for more details).

Source	$\text{H}^{13}\text{CO}^+$		$\text{DCO}^+$		$\text{oH}_2\text{D}^+$		$\text{C}^{18}\text{O}$	
	$T_{\text{ex}}$ K	$N_{\text{col}}$ $10^{11} \text{ cm}^{-2}$	$T_{\text{ex}}$ K	$N_{\text{col}}$ $10^{11} \text{ cm}^{-2}$	$T_{\text{ex}}$ K	$N_{\text{col}}$ $10^{13} \text{ cm}^{-2}$	$T_{\text{ex}}$ K	$N_{\text{col}}$ $10^{15} \text{ cm}^{-2}$
Tau 410	7.5	$1.28 \pm 0.10$	10.8	$0.88 \pm 0.12$	10.8	$0.18 \pm 0.03$	11.4	$0.816 \pm 0.019$
Tau 420	$28 \pm 9$	$0.89 \pm 0.08$	$9.4 \pm 0.4$	$6.0 \pm 0.5$	9.4	$0.24 \pm 0.04$	12.8	$1.45 \pm 0.02$
TMC1-C	7.5	$1.18 \pm 0.10$	10.7	$1.43 \pm 0.17$	10.7	$0.070 \pm 0.013$	11.3	$1.22 \pm 0.02$
L1544	6.7	$2.5 \pm 0.2$	9.6	$4.87 \pm 0.18$	9.6	$0.98 \pm 0.08$	10.2	$1.16 \pm 0.02$
L183	$6.8 \pm 0.6$	$1.5 \pm 0.2$	9.1	$5.22 \pm 0.18$	9.1	$1.28 \pm 0.08$	9.6	$1.68 \pm 0.02$
L429	$5.4 \pm 0.3$	$4.3 \pm 0.7$	9.3	$8.9 \pm 0.3$	9.3	$1.35 \pm 0.06$	9.9	$1.11 \pm 0.03$
L694-2	$5.6 \pm 0.5$	$3.3 \pm 0.7$	9.3	$5.7 \pm 0.2$	9.3	$0.72 \pm 0.06$	9.8	$1.31 \pm 0.03$
Oph 1	$5.2 \pm 0.4$	$3.0 \pm 0.7$	$6.7 \pm 0.3$	$13 \pm 2$	6.7	$1.76 \pm 0.14$	13.4	$2.20 \pm 0.05$
Oph 2	$6.0 \pm 0.3$	$7.6 \pm 0.8$	$10.2 \pm 0.3$	$17.1 \pm 0.8$	10.2	$0.46 \pm 0.03$	13.3	$3.20 \pm 0.03$
Oph 3 <sup>(a)</sup>	-	$22.5 \pm 1.8$	-	$26.8 \pm 1.5$	-	$0.20 \pm 0.08$	-	$6.20 \pm 0.14$
Oph 4 <sup>(a)</sup>	-	$15.6 \pm 1.3$	-	$28 \pm 3$	-	$1.0 \pm 0.3$	-	$8.5 \pm 0.4$
Oph 5	$6.3 \pm 0.2$	$11.0 \pm 1.0$	$5.90 \pm 0.05$	$119 \pm 10$	5.9	$2.34 \pm 0.18$	13.9	$9.11 \pm 0.08$
Oph 6	$6.0 \pm 0.2$	$18.1 \pm 1.6$	$10.3 \pm 0.2$	$27.7 \pm 1.3$	10.3	$0.50 \pm 0.04$	13.8	$5.81 \pm 0.04$
Oph D	$5.6 \pm 0.3$	$8.1 \pm 1.6$	$9.9 \pm 0.3$	$12.8 \pm 0.8$	9.9	$0.69 \pm 0.05$	13.3	$1.67 \pm 0.03$
CrA 038	$8.3 \pm 0.3$	$8.0 \pm 0.5$	$11.6 \pm 0.3$	$11.1 \pm 0.5$	11.6	$0.65 \pm 0.03$	13.7	$7.10 \pm 0.12$
CrA 040	$9.6 \pm 0.2$	$21.2 \pm 0.7$	$13.7 \pm 0.4$	$14.5 \pm 0.5$	13.7	$0.126 \pm 0.014$	15.5	$6.42 \pm 0.04$
CrA 047	$14.5 \pm 0.3$	$24.3 \pm 0.4$	$16.2 \pm 0.6$	$9.0 \pm 0.3$	16.2	$< 0.37$	19.0	$11.73 \pm 0.11$
CrA 044	$12.4 \pm 0.2$	$20.9 \pm 0.4$	$22.2 \pm 0.8$	$7.28 \pm 0.13$	22.2	$< 0.19$	18.2	$10.63 \pm 0.09$
CrA 050	$10.5 \pm 0.4$	$7.6 \pm 0.4$	$14.9 \pm 1.1$	$2.8 \pm 0.2$	14.9	$< 0.38$	18.0	$5.91 \pm 0.08$
CrA 151	$6.4 \pm 0.4$	$5.7 \pm 0.8$	$12.5 \pm 0.3$	$9.8 \pm 0.4$	12.5	$0.52 \pm 0.06$	11.2	$2.47 \pm 0.04$

**Notes.** <sup>(a)</sup> The column densities in Oph 3 and Oph 4 are summed over the two velocity components; the excitation temperatures are, hence, not given.

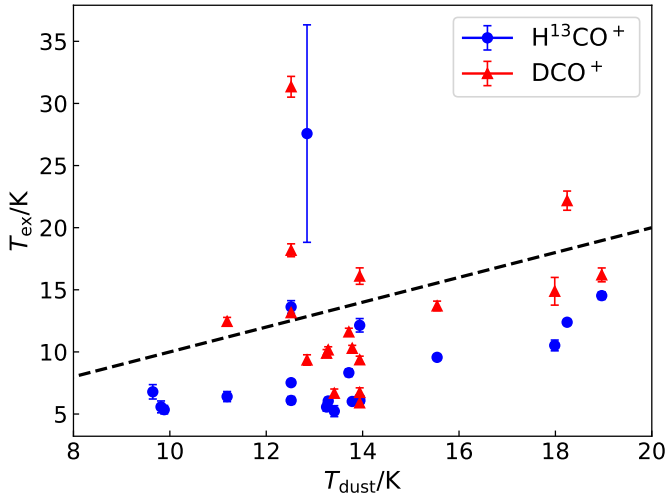


**Fig. 2.**  $T_{\text{ex}}$  of  $\text{H}^{13}\text{CO}^+$  (blue circles) and  $\text{DCO}^+$  (red triangles) for all cores where two transitions of the species are available, as a function of  $T_{\text{dust}}$  values. The dashed black line shows the 1:1 relation. For cores where two velocity components are identified and fitted, we show the parameters of both.

and  $\text{HC}^{18}\text{O}^+$  transitions (with equal  $J$ ) to the expected value  $557/68 = 8.2$ . This is appropriate as the two lines have similar spectroscopic constants (see Table 2), and they are optically thin (see previous subsection). We computed integrated intensities over  $N_{\text{ch}}$  channels with  $\text{S/N} > 3$  signal in the velocity range

$2.8 - 13.5 \text{ km s}^{-1}$ . The associated uncertainties are estimated via  $\sigma_{\text{II}} = \text{rms} \times \Delta V_{\text{ch}} \times \sqrt{N_{\text{ch}}}$ . The result is presented in Fig. 5.

The observed  $\text{H}^{13}\text{CO}^+/\text{HC}^{18}\text{O}^+$  values are in the range 3.5 – 32, with a weighted average of 8.0, very close to the expected value  $557/68 = 8.2$ . The highest values found in the sample are characterised by the highest uncertainties, as they come from sources where the  $\text{HC}^{18}\text{O}^+$  flux has a low  $\text{S/N} = 3 - 5$ . For 50% of cases, the measured value is consistent with the expected one, and in 83% of the sample the value is consistent with a variation of a factor of 2. Given the uncertainties, we conclude that the isotopic ratios we assumed in the analysis are robust.

#### 4.3.3. Beam filling factor

When computing column densities, we assumed a beam filling factor  $\eta_{\text{ff}} = 1$ , which means that the molecular emission is more extended than the APEX angular resolution. This needs to be verified, as column densities will be underestimated if  $\eta_{\text{ff}} < 1$  (beam-dilution). At the frequencies of interest, the APEX angular resolution spans the range  $16 - 35''$ , which corresponds to  $1800 - 3800 \text{ au}$  and  $4000 - 8800 \text{ au}$  for the closest and farthest target, respectively.

Since we do not have available maps to check the real extension of the molecular emission, we have instead examined available data from similar sources. For instance, Keown et al. (2016) reported multi-pointing detection of  $\text{DCO}^+$  (3-2) in L492 and L694-2 (the latter is also present in our sample), and the emission appears well extended beyond  $10000 \text{ au}$ . A similar extension is seen also in L1544 (Redaelli et al. 2019). Emission extended



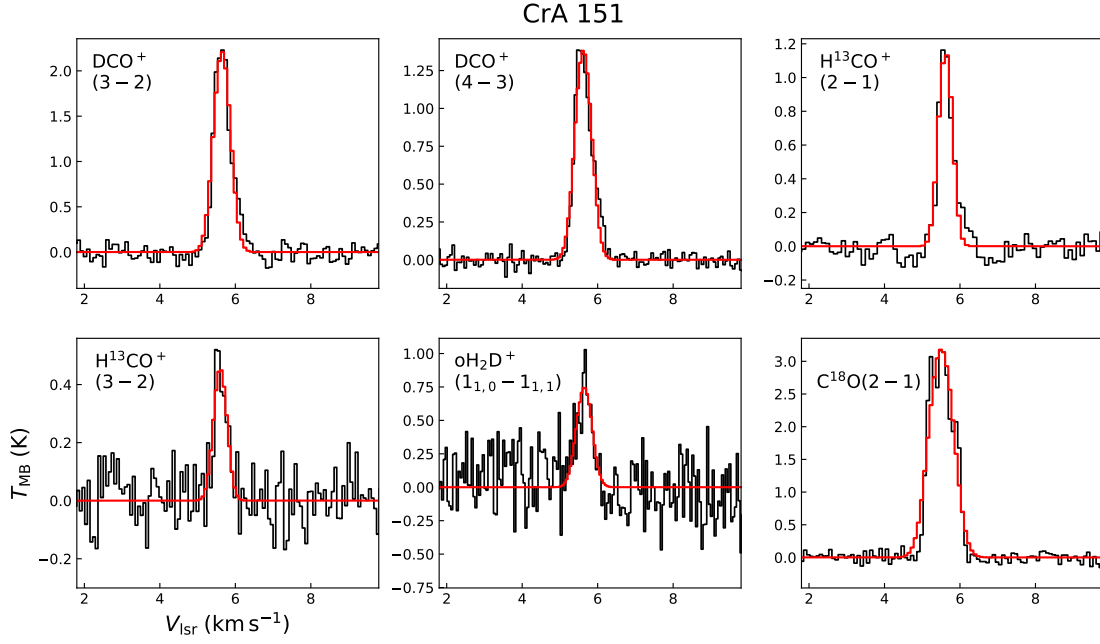


**Fig. 3.** The black histograms show the spectra collected towards CrA 151. The transitions are labelled in the top-left corner of each panel. The red histograms show the best-fit solution of the spectral fit performed as described in Sect. 4.2.

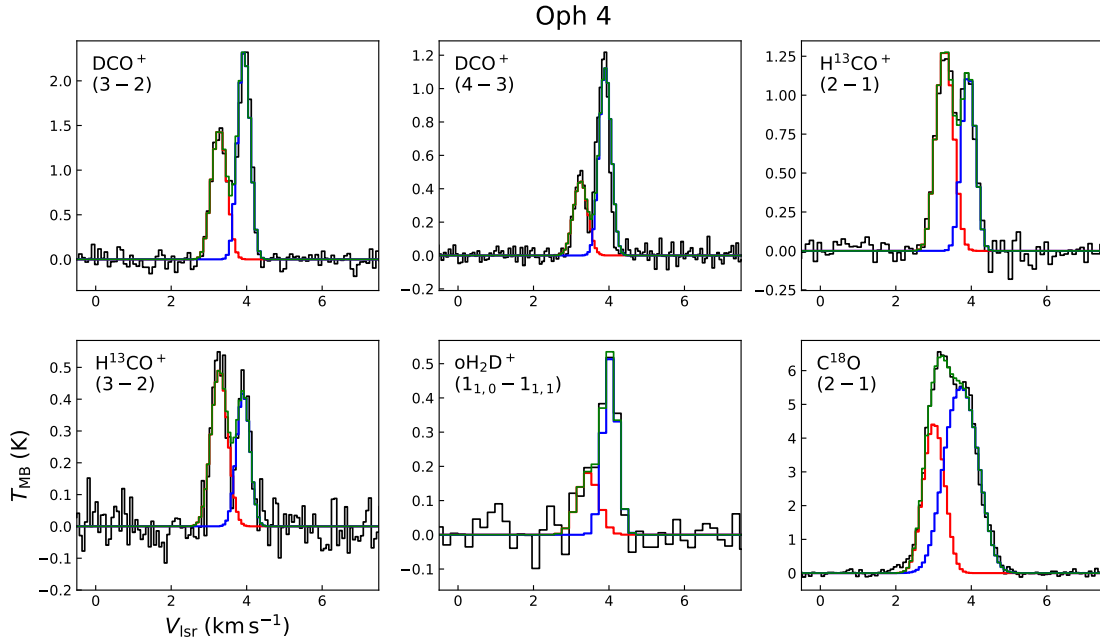


**Fig. 4.** Same as Fig. 3, but for Oph 4. In this core, two velocity components are seen in all the transitions, and we fit them separately. The red/blue curves show the individual best-fit solutions, whilst the green curve represents the total fit.

over several thousands of au is often reported for  $\text{H}^{13}\text{CO}^+$ , even though most studies focus on the (1-0) transition (see e.g. B68, Maret & Bergin 2007; L1498, Maret et al. 2013; several cores in the L1495 filament, Punanova et al. 2018).  $\text{C}^{18}\text{O}$  is an abundant species, which combined with the low critical density of the (2-1) transition makes its emission likely extended (cf. the SEDIGISM survey that used this line to map the ISM in the inner Galaxy, Schuller et al. 2021).

The case of  $\text{oH}_2\text{D}^+$  is more complex, as few maps of this species have been observed in the low-mass regime, to our knowledge. Vastel et al. (2006) mapped the  $\text{oH}_2\text{D}^+(1_{1,0} - 1_{1,1})$

transition in L1544 with the CSO telescope (angular resolution  $20''$ ), and detected it over several beams. The map obtained towards Ophiuchus A SM1N with the James Clark Maxwell Telescope (JCMT) shows emission over  $\sim 5000$  au around the core (Friesen et al. 2014). In Ophiuchus HMM1, Harju et al. (2024) used APEX/LAsMA to map the  $\text{oH}_2\text{D}^+(1_{1,0} - 1_{1,1})$  line, which is emitted over more than 10000 au. We conclude that it is reasonable to expect this transition to fill the  $16''$  APEX beam in the majority of our targets. This is further supported by the fact that for eight cores in the sample, we detected the line not only in the



central LAsMA beam, but also in some of the external beams (which are separated by  $40''$ ).

Even though we can safely exclude beam-dilution issues, we stress that the difference in beam size at different frequencies might cause the underestimation of the column density of some tracers with respect to that of  $\text{oH}_2\text{D}^+$ , which presents the highest resolution. In the final results this problem is mitigated by the fact that the underestimated column densities appear in Eq. 1 as ratios of quantities estimated at similar resolution ( $R_D$  from the  $\text{H}^{13}\text{CO}^+$  and  $\text{DCO}^+$  lines at 2 and 1 mm, and  $X(\text{CO})$  from CO observations at  $\sim 30''$  resolution and *Herschel* maps at  $37''$ ). We cannot exclude, however, the underestimation of  $\zeta_2$  due to that of  $N_{\text{col}}(\text{oH}_2\text{D}^+)$ .

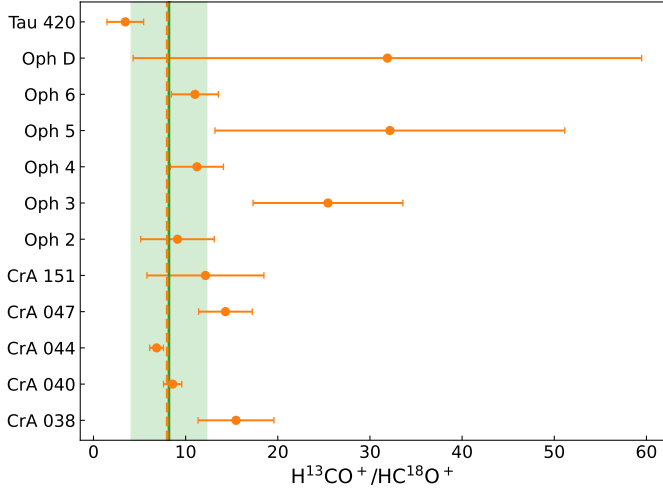


**Fig. 5.** The orange points show the measured flux ratio between the  $\text{H}^{13}\text{CO}^+$  and  $\text{HC}^{18}\text{O}^+$  ( $2-1$ ) lines, in those cores where both transitions are detected (labelled on the y-axis). Errorbars show the  $3\sigma$  level. The vertical dashed orange line is the weighted average of the sample. The expected value  $557/68 = 8.2$  is shown with the vertical green line, and the shaded green area shows a variation of a factor 2 around it.

#### 4.4. Deuteration levels and CO depletion factor

We used the column density values obtained in Sect. 4.2 to compute the deuteration level and the CO abundance in each target. From the latter, we computed the CO depletion factor  $f_D = X^{\text{st}}(\text{CO})/X(\text{CO})$ , where  $X^{\text{st}}(\text{CO}) = 1.2 \times 10^{-4}$  is the standard abundance of undepleted CO (Lee et al. 1996; Pineda et al. 2010; Luo et al. 2023). The values are summarised in Table 4, and their correlation is shown in Fig. 6.

The  $\text{HCO}^+$  deuteration factors are in the range  $0.5 - 15\%$ , with an average value of  $3.4\%$ . Our measured values are in line with other studies of prestellar and starless cores (cf. Butner et al. 1995; Tiné et al. 2000). For a direct comparison of individual targets, our derived value ( $2.8\%$ ) in L1544 is consistent with previous result by Redaelli et al. (2019) ( $3.5\%$ ); in L183, our value of  $5.2 \pm 0.8\%$  is in agreement with the range  $3 - 5\%$  reported by Juvela et al. (2002). The CO depletion factors in our sample are in the range  $1.3 - 21$ , typical for cold and dense cores, as found by Bacmann et al. (2002); Crapsi et al. (2005); Lippok et al. (2013).

Both these quantities are strongly correlated with the core dust temperature, as can be seen in Fig. 6, where the colour scale of the data points is determined by the dust temperature value derived with *Herschel*. The lowest deuteration and depletion values are found in cores where  $T_{\text{dust}} > 15$  K, becom-

ing comparable to the CO desorption temperature ( $\approx 20$  K, cf. Öberg et al. 2011). This immediately lowers the CO depletion factor and, in this physical conditions, the efficiency of deuteration processes is also lowered (Dalgarno & Lepp 1984; Ceccarelli et al. 2014a). The highest deuteration level is found in Oph 5, which presents an intermediate temperature within the sample ( $T_{\text{dust}} = 13.9$  K). However, we highlight that the molecular line emission towards this source presents hints of double-velocity components that cannot be fit for all species (cf. the figure in Appendix A). We highlight that in the sources with the lowest  $f_D$  values, Eq. 1 might underestimate the  $\zeta_2$  value. This, however, does not change the results of our analysis (see Sect. 5).

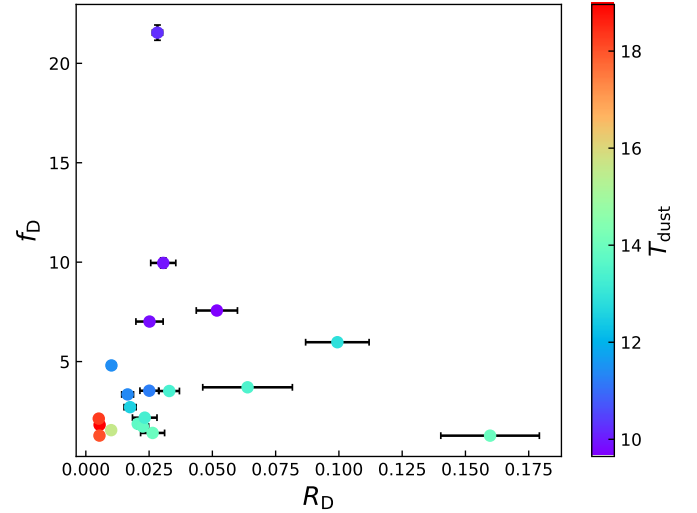


**Fig. 6.** CO depletion factor  $f_D$  as a function of the  $\text{HCO}^+$  deuteration fraction  $R_D$  in the whole sample. The colorscale is determined by the dust temperature value as reported in Table 1.

#### 4.5. Estimates of $\zeta_2$

Using the  $R_D$  and  $X(\text{CO})$  values, we applied Eq. (1) to infer the cosmic-ray ionisation rate values. We initially assumed a value of  $L = 0.1$  pc for the source size, which is often regarded as a typical size of low-mass cores in the local ISM (cf. Andre et al. 2000; Pineda et al. 2023). A further discussion on the choice of this parameter is presented later. The obtained values and associated uncertainties are reported in the fourth column of Table 4 and in Fig. 7, as a function of the total gas column density  $N(\text{H}_2)$  (upper panel). In the three sources (CrA 044, 047, and 050) where  $\text{oH}_2\text{D}^+$  is not detected, we report  $3\sigma$  upper limits of  $\zeta_2$ . The  $\zeta_2$  values are scattered over almost two orders of magnitude, ranging from a minimum of  $1.3 \times 10^{-18} \text{ s}^{-1}$  to a maximum of  $8.5 \times 10^{-17} \text{ s}^{-1}$  (excluding the upper limits). The scatter is significantly larger than the intrinsic uncertainty of the method (estimated as a factor of  $2 - 3$ , see Redaelli et al. 2024). We discuss possible explanations for the observed scatter in Sect. 5.

The choice of the  $L$  value is crucial, as the analytic expression for  $\zeta_2$  is inversely proportional to it. The topic has been discussed lengthily in Bovino et al. (2020) and Redaelli et al. (2024). A possible approach is to estimate  $L$  from the maps of total column density presented in Sect. 4.1, using the equivalent radius computed from a given contour of  $N(\text{H}_2)$ . Choosing which contour is, however, not straightforward. The cores present different contrast levels, i.e. the ratio between the peak  $N(\text{H}_2)$  value

**Table 4.** List of  $\text{HCO}^+$  deuteration fractions, CO depletion factors, and  $\zeta_2$  values obtained across the sample. The last column reports the range of  $\zeta_2$  values obtained when using different  $N(\text{H}_2)$  contours to estimate  $L$ .

Source	$R_D$ $\times 10^{-2}$	$f_D$	$\zeta_2/10^{-17} \text{ s}^{-1}$	
			$L = 0.1 \text{ pc}$	$L \text{ from } 40\text{-}60\% \text{ } N(\text{H}_2)$
Tau 410	$1.01 \pm 0.16$	$4.81 \pm 0.11$	$1.2 \pm 0.3$	$0.8 - 1.2$
Tau 420	$9.9 \pm 1.3$	$5.97 \pm 0.09$	$0.13 \pm 0.03$	$0.1 - 0.2$
TMC1-C	$1.7 \pm 0.2$	$3.35 \pm 0.06$	$0.40 \pm 0.09$	$0.25 - 0.31$
L1544	$2.8 \pm 0.2$	$21.5 \pm 0.4$	$0.51 \pm 0.06$	$0.4 - 0.7$
L183	$5.2 \pm 0.8$	$7.57 \pm 0.11$	$1.05 \pm 0.18$	$1.4 - 2.0$
L429	$3.1 \pm 0.5$	$10.0 \pm 0.3$	$1.4 \pm 0.2$	$1.3 - 2.2$
L694-2	$2.5 \pm 0.5$	$7.01 \pm 0.14$	$1.3 \pm 0.3$	$1.2 - 1.7$
Oph 1	$6.4 \pm 1.8$	$3.71 \pm 0.08$	$2.3 \pm 0.7$	$1.6 - 3.4$
Oph 2	$3.3 \pm 0.4$	$3.52 \pm 0.03$	$1.21 \pm 0.17$	$1.1 - 1.6$
Oph 3	$1.8 \pm 0.2$	$2.71 \pm 0.09$	$1.3 \pm 0.7$	$1.2 - 1.5$
Oph 4	$2.6 \pm 0.5$	$1.41 \pm 0.09$	$8 \pm 4$	$5.9 - 10.1$
Oph 5	$16 \pm 2$	$1.274 \pm 0.012$	$3.5 \pm 0.5$	$2.8 - 4.3$
Oph 6	$2.3 \pm 0.2$	$1.732 \pm 0.013$	$3.9 \pm 0.5$	$2.5 - 3.3$
Oph D	$2.3 \pm 0.5$	$2.18 \pm 0.04$	$4.1 \pm 0.9$	$3.8 - 5.4$
CrA 038	$2.05 \pm 0.15$	$1.87 \pm 0.03$	$5.1 \pm 0.5$	$4.7 - 6.6$
CrA 040	$1.00 \pm 0.05$	$1.550 \pm 0.010$	$2.4 \pm 0.3$	$1.7 - 2.1$
CrA 044	$0.511 \pm 0.014$	$2.13 \pm 0.02$	$< 5.05$	$< 6.8 - 11.5$
CrA 047	$0.544 \pm 0.019$	$1.82 \pm 0.02$	$< 10.8$	$< 15.3 - 24.6$
CrA 050	$0.54 \pm 0.05$	$1.28 \pm 0.02$	$< 16.2$	$< 12.2 - 15.1$
CrA 151	$2.5 \pm 0.4$	$3.53 \pm 0.06$	$1.9 \pm 0.4$	$2.4 - 4.5$

at the core's centre and the surrounding average  $N(\text{H}_2)$  varies significantly, from a factor of a few to more than one order of magnitude. Furthermore, several cores are embedded in crowded environments (in particular, in Ophiuchus and Corona). The selection of closed  $N(\text{H}_2)$  contours is, hence, highly dependent on the cores' parental environments. To take into account the uncertainty associated with the  $L$  value, we have computed the equivalent diameter corresponding to 40% and 60% of the  $N(\text{H}_2)$  peak at the cores' position. These levels lead to close contours in the whole sample. These values are presented in Table 1. We then computed a range of corresponding  $\zeta_2$ , using the range of  $L$  values in Eq. 1, and we report them in the last column of Table 4 and in the upper panel of Fig. 7 using shaded points. For most sources, the  $\zeta_2$  value obtained using  $L = 0.1 \text{ pc}$  is consistent, within uncertainties, with the range of values computed adopting a variable  $L$ , with only three exceptions (CrA 151, L183, and Oph 6)<sup>7</sup>.

A second possibility to infer  $L$  is to use the detected lines to trace the total gas volume density and, thus,  $L = N(\text{H}_2)/n(\text{H}_2)$ . In Appendix B we perform LVG modelling of the  $\text{H}^{13}\text{CO}^+$  transitions, which are available in the majority of the sample. The results show that even if it is true that in several targets the  $n(\text{H}_2)$  values derived from  $L = 0.1 \text{ pc}$  are underestimated, this underestimation is in line with the method's error, and this does not affect the main conclusions of this work. We conclude that the choice of  $L$  will not significantly impact our analysis and results.

#### 4.6. Ionisation degree and dynamical state of the cores

The ionisation degree of the gas is measured by the electron abundance, or electron fraction  $x(\text{e}^-)$ . In the assumption that free electrons are donated by neutral species, and that the charge of dust grains is negligible, one can compute  $x(\text{e}^-)$  by assuming the gas charge balance. Latrille et al. (2025) introduced the following proxy for  $x(\text{e}^-)$ :

$$x(\text{e}^-) = X(\text{H}_3^+) + X(\text{HCO}^+) + X(\text{DCO}^+) + X(\text{N}_2\text{H}^+) + X(\text{N}_2\text{D}^+), \quad (2)$$

where  $X(\text{H}_3^+) = X(\text{oH}_2\text{D}^+)/3R_D$ . The authors tested it on a set of magneto-hydrodynamic simulations, finding that it reproduces the true  $x(\text{e}^-)$  values with a scatter of 0.5 dex. According to the chemical model of those authors, the main contributions to Eq. (2) come from  $\text{H}_3^+$  and  $\text{HCO}^+$ . We used this equation to measure  $x(\text{e}^-)$  in each core of the sample, neglecting the diazenylium terms for which we have no estimate, considering only sources with the detection of  $\text{oH}_2\text{D}^+$ . The obtained values are lower limits to the true gas ionisation degree. Figure 8 shows the resulting plot of  $x(\text{e}^-)$  as a function of the cores' column density.

The obtained values are found in the range  $10^{-9} - 10^{-8}$ , with the majority of cores showing an ionisation degree of  $2 - 4 \times 10^{-9}$ . These values are in line with literature results in similar sources (Caselli et al. 2002; Maret & Bergin 2007), but they are substantially lower than those derived in NGC1333 by Pineda et al. (2024).

The ionisation degree is directly proportional to the timescale for ambipolar diffusion  $t_{\text{AD}}$ , i.e. the process of drift between the neutral species and the ionised one due to imperfect coupling between the two gas flows. In particular,  $t_{\text{AD}}$  can be computed as (Spitzer 1978; Shu et al. 1987):

<sup>7</sup> Here, we do not take into considerations the three sources with upper limits on  $\text{oH}_2\text{D}^+$ .

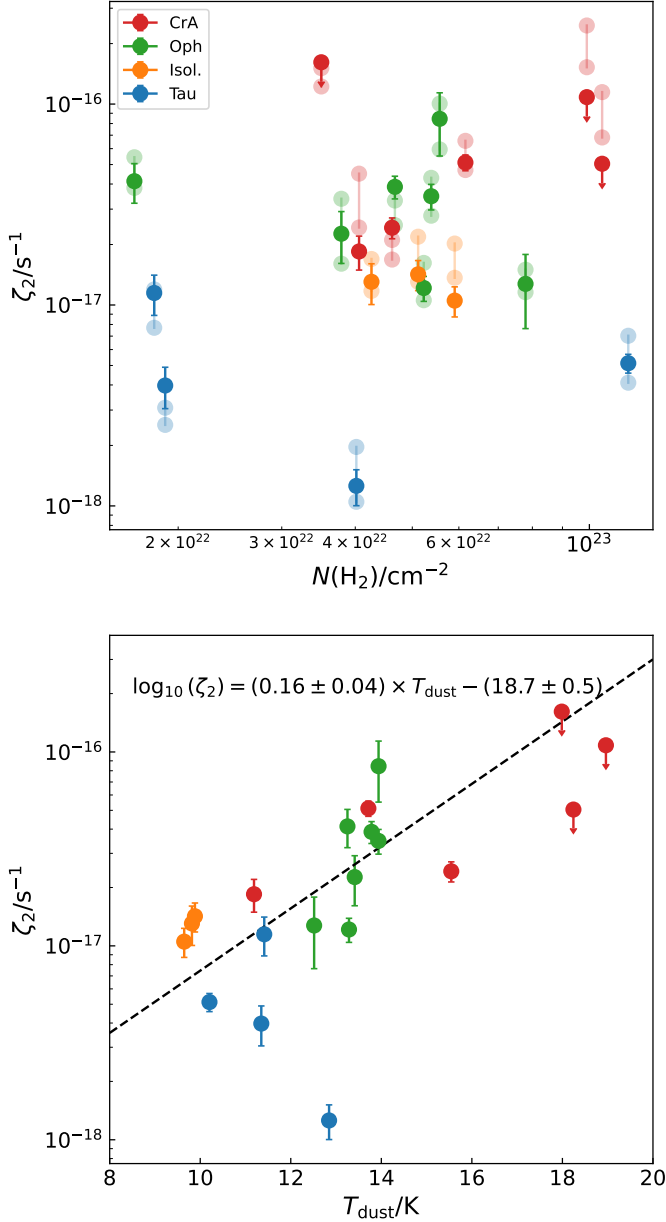


**Fig. 7.** *Upper panel:* The obtained  $\zeta_2$  values are plotted as a function of the total gas column density towards each core (including the column density integrated along the line of sight). The solid points and error bars are computed using  $L = 0.1$  pc. The upper limits are shown with downward arrows. The transparent points show the range of  $\zeta_2$  values obtained when  $L$  is computed using the 40% or 60% contours of  $N(\text{H}_2)$ , as described in the Main Text. *Lower panel:* The  $\zeta_2$  values (computed for  $L = 0.1$  pc) are plotted as a function of the cores' dust temperature, as derived from the *Herschel* maps. The dashed line shows the linear regression computed in the  $\log_{10}(\zeta_2)$ - $T_{\text{dust}}$  plane, and the computed regression coefficients are shown at the top of the panel. In both panels, the data-points are colour-coded by parental cloud (red: Corona Australis, green: Ophiuchus, blue: Taurus, orange: Isolated sources).

$$t_{\text{AD}} = 2.5 \times 10^{13} \times x(\text{e}^-) \text{ yr}. \quad (3)$$

We have used the computed values of  $x(\text{e}^-)$  to estimate  $t_{\text{AD}}$  in each core. These values are also lower limits. We compare them to the free-fall timescales ( $t_{\text{ff}}$ ), to assess the dynamical stability

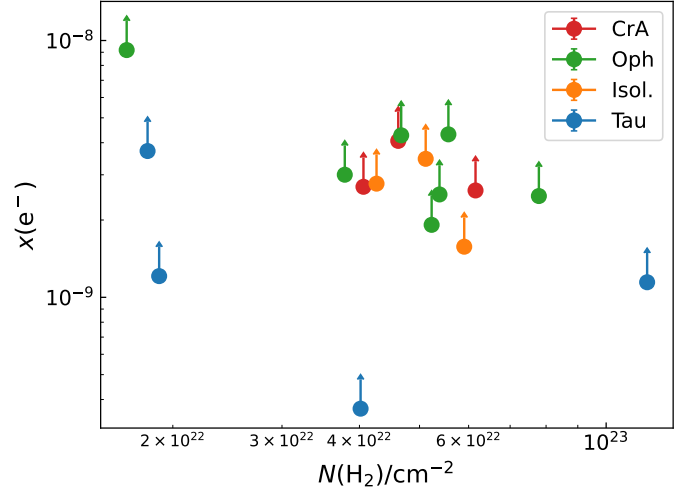


**Fig. 8.** Estimation of the ionisation fraction  $x(\text{e}^-)$  using Eq. (2), as a function of the cores' central total column densities, in the targets with detected  $\text{oH}_2\text{D}^+$  emission. We neglected the contribution of  $\text{N}_2\text{H}^+$  and  $\text{N}_2\text{D}^+$ . As in Fig. 7, the data-points are colour-coded according to the parental cloud.

of the cores:

$$t_{\text{ff}} = \sqrt{\frac{3\pi}{32 G \mu m_{\text{H}} n(\text{H}_2)}}. \quad (4)$$

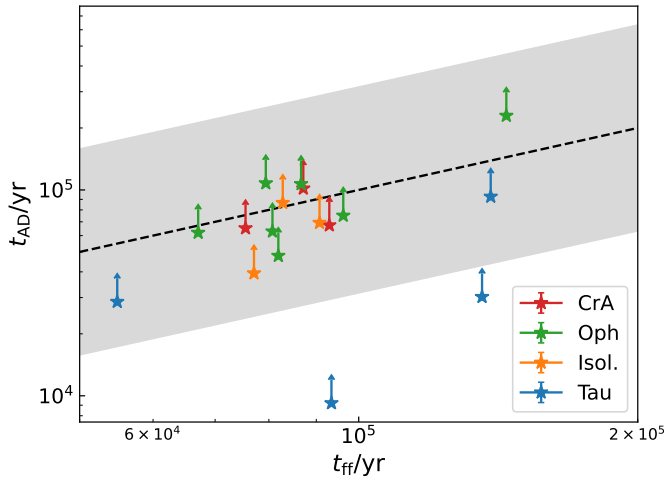
We adopt  $\mu = 2.33$  for the mean molecular weight of the gas and  $n(\text{H}_2) = N(\text{H}_2)/0.1$  pc, using the  $N(\text{H}_2)$  tabulated values reported in Table 1. We stress that this approach is underestimating the true central densities of the cores, because it involves a column density value that is averaged on the *Herschel* beam size and it assumes that the volume density is constant along the line of sight. However, in Appendix B we show that the underestimation is likely of a factor of  $\sim 2$ , and it does not affect the whole sample.

Figure 9 compares the ambipolar diffusion and free-fall timescales in all the sources. Considering the limitations of the method, we can conclude that the derived  $t_{\text{AD}}$  values are on average consistent with, or larger than, the corresponding  $t_{\text{ff}}$ . For the Oph 1-6 cores, this is in line with Bovino et al. (2021), who found that these sources are consistent with model of fast collapse on shorter timescales than the ambipolar diffusion ones.

## 5. Discussion

### 5.1. The role of the environment

The resulting  $\zeta_2$  values shown in Fig. 7 are coloured by parental cloud. A trend can be seen: cores in Ophiuchus and Corona Australis present on average higher ionisation rates than in Taurus or in the more isolated cores (L183, L694-2, and L429, which is found close to the Aquila Rift). The weighted averages in each environment (excluding upper limits) are  $\langle \zeta_2 \rangle = (2.8 \pm 0.2) \times 10^{-17} \text{ s}^{-1}$  in Corona,  $(1.76 \pm 0.14) \times 10^{-17} \text{ s}^{-1}$  in Ophiuchus,  $(0.23 \pm 0.03) \times 10^{-17} \text{ s}^{-1}$  in Taurus, and  $(1.22 \pm 0.12) \times 10^{-17} \text{ s}^{-1}$  for the three more isolated sources. The differences, in particular between Taurus and Ophiuchus or Corona, are significant considering both the uncertainties reported in Table 4 and the intrinsic error of the method. This points toward the role of the environmental properties in setting the average ionisation rate at



**Fig. 9.** Scatterplot of the ambipolar diffusion timescale  $t_{AD}$  as a function of the free-fall time  $t_{ff}$  in the targets with detected  $\text{oH}_2\text{D}^+$  emission. The  $t_{AD}$  values are lower limits as  $x(e^-)$  estimated from (2) represents a lower limit. The datapoints are color-coded by environment, as in Fig. 7. The dashed line is the 1:1 relation, whilst the shaded area is a 0.5dex scatter around it (corresponding to the deviation of Eq. 2 from the true value estimated by Latrille et al. (2025)).

the core scales. A similar conclusion was also reached by Sabatini et al. (2023) in high-mass star-forming regions, where the authors highlighted that cores embedded in the same parental clump showed similar  $\zeta_2$  values, whilst significant differences were found when comparing distinct clumps.

We have investigated which environmental physical parameters have the strongest influence on the overall ionisation rate of the cores. From the upper panel of Fig. 7, it appears that the differences in column density among these cores may not be the primary factor contributing to the variations in  $\zeta_2$ . There is no clear correlation between  $\zeta_2$  and  $N(\text{H}_2)$ , and the cores embedded in different clouds cover similar ranges of  $N(\text{H}_2)$  values. On the other hand, the regions analysed differ by dust temperature. Looking at the values in Table 1, the cores' temperatures are 11 – 19 K in Corona,  $\sim 13.5$  K in Ophiuchus, 10 – 13 K in Taurus and  $< 10$  K in the three isolated sources. The trend is shown in the lower panel of Fig. 7, where we show also the linear regression fit to the values (upper limits excluded) in the semi-logarithmic plane. The Spearman correlation coefficient is 0.65, indicating a high probability of positive correlation between the two quantities. The associated  $p$ -value is  $0.004 \ll 0.05$ , hence rejecting the null-hypothesis that the two quantities are not correlated. In Appendix B we show that the correlation remains valid when the gas volume density and the  $L$  parameter are inferred from the molecular data, instead of the *Herschel* data.

The different temperatures can be linked to the star-formation activity in the regions. Five of the six cores selected in Corona are found in the proximity of the so-called Coronet cluster, which hosts several YSOs at distinct evolutionary stages (cf. Chini et al. 2003; Sicilia-Aguilar et al. 2013). For CrA 044, 047, and 050 (the latter a known protostellar core) we report only upper limits on  $\text{oH}_2\text{D}^+$  and  $\zeta_2$ . This is because the higher temperatures caused by the nearby protostellar activity favour the CO desorption from the dust grains back to the gas phase, as shown by the low values of CO depletion we measured ( $f_D = 1 - 2$ ). CO, in turn, quickly destroys  $\text{H}_2\text{D}^+$ . The lowest  $\zeta_2$  value in the Corona cores is found in CrA 151, which is located  $\sim 5$  pc away from the Coronet cluster region and is a quiescent core with high

levels of deuteration (Redaelli et al. 2025). Ophiuchus is also a very active star-forming region, with approximately  $\sim 300$  YSO sources identified (Dunham et al. 2015). On the contrary, the cores in Taurus and the isolated sources are found in relatively quieter environments, as proved by both the low temperature values and the low line velocity dispersions found in these cores (cf. Table A.1). The main exception is L429, close to the active region of the Aquila Rift. In further support to the scenario just described, L429 presents the highest  $\zeta_2$  value in this subset, even though the difference is within the uncertainties.

The correlation between the star-formation activity and the ionisation rate of the gas is supported by recent theoretical works, which showed that low-mass protostars can be a source of local re-acceleration of cosmic rays (Padovani et al. 2015, 2016), either at the protostellar surface or in the shocks along the protostellar jets. This can explain the detection of non-thermal radiation in these jets (cf. Ainsworth et al. 2014). Regions with strong protostellar activity, therefore, might be characterised by higher levels of ionisation due to CRs, as first noted by Ceccarelli et al. (2014b) and seen also in the maps of Pineda et al. (2024). Based on YSOs count, Heiderman et al. (2010) and Evans et al. (2014) estimated the surface density of star formation  $\Sigma(SFR)$  in several Gould Belt Clouds, and reported values of  $2.44 \text{ M}_\odot \text{ yr}^{-1} \text{ kpc}^{-2}$  in Ophiuchus, 3.47 in Corona, and 0.15 in Taurus, respectively, which further supports the scenario of correlation between star formation activity and average ionisation level.

## 5.2. Comparison with current models of CR propagation

In this Section, we discuss the obtained results in the context of available measurements of the CR ionisation rate in the Milky Way and in comparison with the prediction of theoretical models of CR propagation and attenuation. Figure 10 shows a summary of observational estimates taken from literature, as a function of the sources  $N(\text{H}_2)$ , with a particular focus on those obtained using the same method we implemented. The only exception is the values at low densities ( $N(\text{H}_2) \lesssim 10^{21} \text{ cm}^{-2}$ ), which refer to diffuse clouds (Obolentseva et al. 2024). These estimates have been re-evaluated  $\zeta_2$  using 3D visual extinction maps to infer the volume densities of the sources. As a result, they are on average a factor of 9 lower than previous estimates (Indriolo et al. 2007; Indriolo & McCall 2012). The new values obtained in this work are shown with orange stars.

The plots also show the expected trends for the total ionisation rate computed assuming different models of the energy spectrum of protons from Padovani et al. (2022): model low ( $\mathcal{L}$ ), high ( $\mathcal{H}$ ), and the upper-limit model  $\mathcal{U}$  that adopts a steep spectral slope  $\alpha = -1.2$ . The high model was introduced initially with the scope of explaining the high  $\zeta_2$  values obtained in diffuse clouds from  $\text{H}_3^+$  measurements, and it might not be needed anymore given the results of Obolentseva et al. (2024). As discussed in the previous subsection, we do not see a significant decreasing trend with  $N(\text{H}_2)$ , as the correlation with the environmental temperature (measured by means of  $T_{\text{dust}}$ ) is stronger. We also highlight, however, that we explored a relatively small range of column density (less than one order of magnitude). Most of our values are found across the  $\mathcal{L}$  model, which is the one in agreement with the Voyager data. Nevertheless, we obtained a significant scatter, both towards low and towards high values. As noted before, we hypothesise that environmental effects are the main driver for it. This strengthens the idea that a universal  $\zeta_2$  value cannot be adopted even for sources with similar properties and evolutionary stage.



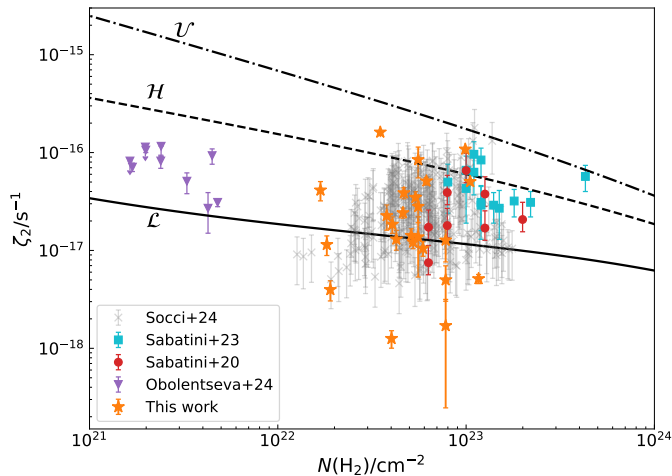


**Fig. 10.**  $\zeta_2$  as a function of  $N(\text{H}_2)$ . The theoretical models  $\mathcal{L}$  (solid black line),  $\mathcal{H}$  (dashed black line), and  $\mathcal{M}$  (dotted-dashed black line) are taken from Padovani et al. (2022). The new observational estimates obtained in this work are shown with orange stars. The most recent values in the diffuse gas are shown with purple triangles (Obolentseva et al. 2024). We also show literature values in dense gas obtained with the method of Bovino et al. (2020), represented with red dots (Sabatini et al. 2020), cyan squares (Sabatini et al. 2023), and shaded grey crosses (Socci et al. 2024).

## 6. Summary and Conclusions

In this work, we estimated the CR ionisation rate  $\zeta_2$  in a sample of dense and cold cores embedded in different star-forming regions in the Solar neighbourhood. We employed the analytical method of Bovino et al. (2020), further corroborated and updated by Redaelli et al. (2024), which correlates  $\zeta_2$  with the column density of  $\text{oH}_2\text{D}^+$ , the CO abundance, and the deuteration fraction of  $\text{HCO}^+$ . To estimate these quantities, we analysed new, high-sensitivity spectroscopic data observed with the APEX single-dish telescope. Furthermore, we used the column density and dust temperature maps obtained from the analysis of the *Herschel* data to characterise the cores' average  $N(\text{H}_2)$  and  $T_{\text{dust}}$  values.

We performed a spectral fit to the observed transitions to infer the molecular column density, assuming C-TEX conditions. The estimated deuteration fractions are in the range 0.5 – 15% and the CO depletion factors span the range  $f_{\text{D}} = 1.3 - 21$ , which are in agreement with expectations from chemical considerations. Both these parameters correlate with the cores' temperature. As  $T_{\text{dust}}$  increases and approaches the CO desorption temperature ( $\sim 20$  K), the CO molecules return to the gas-phase (decreasing  $f_{\text{D}}$ ) and quickly destroy  $\text{oH}_2\text{D}^+$  and, in general, deuterated species, lowering in turn  $R_{\text{D}}$ .

We infer the  $\zeta_2$  value in 17 cores. For three cores,  $\text{oH}_2\text{D}^+$  was undetected at the sensitivity level of our observations, and we estimated upper limits on  $\zeta_2$ . To our knowledge, this represents the largest sample of  $\zeta_2$  measurements in low-mass dense cores obtained with a consistent methodology after the one presented by Caselli et al. (1998). The  $\zeta_2$  measurements span a range of almost two orders of magnitude, from  $1.3 \times 10^{-18}$  to  $8.5 \times 10^{-17} \text{ s}^{-1}$ . We do not find a significant correlation with the sources' total column density. However, we do find significant differences when comparing cores embedded in distinct environments. We detect a significant positive correlation with the cores' temperature. We speculate that warmer environments are associated with stronger star-formation activity and they are more affected by protostel-

lar feedback, which causes the temperature rise. This is consistent with theoretical predictions on how low-mass protostars can be local sources of re-acceleration of cosmic rays. Our work strongly suggests that the gas ionisation state (which is crucial for several physical and chemical processes) is not a common property even in sources of similar kind and evolutionary stage, and, instead, it varies strongly both due to local and environmental effects. Future efforts dedicated to increasing the sample size to more environments will allow a better understanding of which other environmental properties are important to set the ionisation rate in dense gas.

**Acknowledgements.** The authors gracefully acknowledge Dr. Jorma Harju for his help and support. This publication is based on data acquired with the Atacama Pathfinder Experiment (APEX). APEX has been a collaboration between the Max-Planck-Institut für Radioastronomie, the European Southern Observatory, and the Onsala Space Observatory. This research has made use of data from the Herschel Gould Belt survey (HGBS) project (<http://gouldbelt-herschel.cea.fr>). The HGBS is a Herschel Key Programme jointly carried out by SPIRE Specialist Astronomy Group 3 (SAG 3), scientists of several institutes in the PACS Consortium (CEA Saclay, INAF-IFSI Rome and INAF-Arcetri, KU Leuven, MPIA Heidelberg), and scientists of the Herschel Science Center (HSC). SB acknowledges BASAL Centro de Astrofísica y Tecnologías Afines (CATA), project number AFB-17002. GS acknowledges the project PRIN-MUR 2020 MUR BEYOND-2p (“Astrochemistry beyond the second period elements”, Prot. 2020AFB3FX), the PRIN MUR 2022 FOSSILS (“Chemical origins: linking the fossil composition of the Solar System with the chemistry of protoplanetary disks”, Prot. 2022JC2Y93), the project ASI-Astrobiologia 2023 MIGLIORA (“Modeling Chemical Complexity”, F83C23000800005), the INAF-GO 2023 fundings PRO-TOSKA (“Exploiting ALMA data to study planet forming disks: preparing the advent of SKA”, C13C23000770005) and the INAF-Minigrant 2023 TRIESTE (“TRacing the chemical hEritage of our originS: from proTostars to planEtS”, PI: G. Sabatini). GL gratefully acknowledges the financial support of ANID-Subdirección de Capital Humano/Magister Nacional/2024-22241873 and Millennium Nucleus NCN23\_002 (TITANS). MP acknowledges the INAF-Minigrant 2024 ENERGIA (“ExploriNG low-ENERgy cosmic Rays throuGH theoretical InvestiGAtions at INAF”, PI: M. Padovani). The authors thank the anonymous referee for their comments, which helped improved the quality of the manuscript.

## References

- Ainsworth, R. E., Scaife, A. M. M., Ray, T. P., et al. 2014, *ApJ*, 792, L18
- André, P., Men'shchikov, A., Bontemps, S., et al. 2010, *A&A*, 518, L102
- André, P., Ward-Thompson, D., & Barsony, M. 2000, in *Protostars and Planets IV*, ed. V. Mannings, A. P. Boss, & S. S. Russell, 59
- Bacmann, A., Lefloch, B., Ceccarelli, C., et al. 2002, *A&A*, 389, L6
- Belitsky, V., Bylund, M., Desmaris, V., et al. 2018a, *A&A*, 611, A98
- Belitsky, V., Lapkin, I., Fredrixon, M., et al. 2018b, *A&A*, 612, A23
- Bovino, S., Ferrada-Chamorro, S., Lupi, A., et al. 2019, *ApJ*, 887, 224
- Bovino, S., Ferrada-Chamorro, S., Lupi, A., Schleicher, D. R. G., & Caselli, P. 2020, *MNRAS: Letters*, 495, L7
- Bovino, S., Lupi, A., Giannetti, A., et al. 2021, *A&A*, 654, A34
- Bresnahan, D., Ward-Thompson, D., Kirk, J. M., et al. 2018, *A&A*, 615, A125
- Butner, H. M., Lada, E. A., & Loren, R. B. 1995, *ApJ*, 448, 207
- Caselli, P. & Dore, L. 2005, *A&A*, 433, 1145
- Caselli, P., Vastel, C., Ceccarelli, C., et al. 2008, *A&A*, 492, 703
- Caselli, P., Walmsley, C. M., Terzieva, R., & Herbst, E. 1998, *ApJ*, 499, 234
- Caselli, P., Walmsley, C. M., Zuccconi, A., et al. 2002, *ApJ*, 565, 344
- Ceccarelli, C., Caselli, P., Bockelée-Morvan, D., et al. 2014a, in *Protostars and Planets VI*, ed. H. Beuther, R. S. Klessen, C. P. Dullemond, & T. Henning, 859
- Ceccarelli, C., Dominik, C., López-Sepulcre, A., et al. 2014b, *ApJ*, 790, L1
- Chini, R., Kämpgen, K., Reipurth, B., et al. 2003, *A&A*, 409, 235
- Colzi, L., Sipilä, O., Roueff, E., Caselli, P., & Fontani, F. 2020, *A&A*, 640, A51
- Crapci, A., Caselli, P., Walmsley, C. M., et al. 2005, *ApJ*, 619, 379
- Cummings, A. C., Stone, E. C., Heikkilä, B. C., et al. 2016, *ApJ*, 831, 18
- Dalgarno, A. & Lepp, S. 1984, *ApJ*, 287, L47
- Dunham, M. M., Allen, L. E., Evans, Neal J. I., et al. 2015, *ApJS*, 220, 11
- Edenhofer, G., Zucker, C., Frank, P., et al. 2024, *A&A*, 685, A82
- Evans, Neal J. I., Heiderman, A., & Vutisalchavakul, N. 2014, *ApJ*, 782, 114
- Friesen, R. K., Di Francesco, J., Bourke, T. L., et al. 2014, *ApJ*, 797, 27
- Froebich, D. & Rowles, J. 2010, *MNRAS*, 406, 1350
- Fuente, A., Cernicharo, J., Roueff, E., et al. 2016, *A&A*, 593, A94
- Galli, P. A. B., Bouy, H., Olivares, J., et al. 2020, *A&A*, 634, A98
- Galli, P. A. B., Loinard, L., Bouy, H., et al. 2019, *A&A*, 630, A137

- Ginsburg, A. & Mirocha, J. 2011, PySpecKit: Python Spectroscopic Toolkit, Astrophysics Source Code Library, record ascl:1109.001
- Ginsburg, A., Sokolov, V., de Val-Borro, M., et al. 2022, *AJ*, 163, 291
- Goldsmith, P. F. 2001, *ApJ*, 557, 736
- Guelin, M., Langer, W. D., Snell, R. L., & Wootten, H. A. 1977, *ApJ*, 217, L165
- Guelin, M., Langer, W. D., & Wilson, R. W. 1982, *A&A*, 107, 107
- Güsten, R., Baryshev, A., Bell, A., et al. 2008, in *Millimeter and Submillimeter Detectors and Instrumentation for Astronomy IV*, ed. W. D. Duncan, W. S. Holland, S. Withington, & J. Zmuidzinas, Vol. 7020, International Society for Optics and Photonics (SPIE), 702010
- Güsten, R., Nyman, L. Å., Schilke, P., et al. 2006, *A&A*, 454, L13
- Harju, J., Vastel, C., Sipilä, O., et al. 2024, *A&A*, 688, A117
- Heiderman, A., Evans, Neal J., I., Allen, L. E., Huard, T., & Heyer, M. 2010, *ApJ*, 723, 1019
- Hezareh, T., Houde, M., McCoe, C., Vastel, C., & Peng, R. 2008, *ApJ*, 684, 1221
- Indriolo, N., Geballe, T. R., Oka, T., & McCall, B. J. 2007, *ApJ*, 671, 1736
- Indriolo, N. & McCall, B. J. 2012, *ApJ*, 745, 91
- Juvela, M., Mattila, K., Lehtinen, K., et al. 2002, *A&A*, 382, 583
- Keown, J., Schnee, S., Bourke, T. L., et al. 2016, *ApJ*, 833, 97
- Kirk, J. M., Ward-Thompson, D., Palmeirim, P., et al. 2013, *MNRAS*, 432, 1424
- Kong, S., Caselli, P., Tan, J. C., Wakelam, V., & Sipilä, O. 2015, *ApJ*, 804, 98
- Ladjelate, B., André, P., Könyves, V., et al. 2020, *A&A*, 638, A74
- Latrille, G., Lupi, A., Bovino, S., et al. 2025, *A&A*, 699, A126
- Lee, H. H., Bettens, R. P. A., & Herbst, E. 1996, *A&AS*, 119, 111
- Lippok, N., Launhardt, R., Semenov, D., et al. 2013, *A&A*, 560, A41
- Loison, J.-C., Wakelam, V., Gratier, P., & Hickson, K. M. 2020, *MNRAS*, 498, 4663
- Loison, J.-C., Wakelam, V., Gratier, P., et al. 2019, *MNRAS*, 485, 5777
- Luo, G., Zhang, Z.-Y., Bisbas, T. G., et al. 2023, *ApJ*, 946, 91
- Maret, S. & Bergin, E. A. 2007, *ApJ*, 664, 956
- Maret, S., Bergin, E. A., & Tafalla, M. 2013, *A&A*, 559, A53
- Marsh, K. A., Kirk, J. M., André, P., et al. 2016, *MNRAS*, 459, 342
- McCall, B. J., Huneycutt, A. J., Saykally, R. J., et al. 2003, *Nature*, 422, 500
- Mouschovias, T. C. & Spitzer, L., J. 1976, *ApJ*, 210, 326
- Müller, H. S., Schläder, F., Stutzki, J., & Winnewisser, G. 2005, *Journal of Molecular Structure*, 742, 215, *MOLECULAR SPECTROSCOPY AND STRUCTURE*
- Neufeld, D. A., Welty, D. E., Ivlev, A. V., et al. 2024, *arXiv e-prints*, arXiv:2408.11108
- Öberg, K. I., Murray-Clay, R., & Bergin, E. A. 2011, *ApJ*, 743, L16
- Obolentseva, M., Ivlev, A. V., Silsbee, K., et al. 2024, *arXiv e-prints*, arXiv:2408.11511
- Oka, T. 2019, *Philosophical Transactions of the Royal Society of London Series A*, 377, 20180402
- Ortiz-León, G. N., Loinard, L., Dzib, S. A., et al. 2018, *ApJ*, 869, L33
- Padovani, M., Bialy, S., Galli, D., et al. 2022, *A&A*, 658, A189
- Padovani, M., Galli, D., & Glassgold, A. E. 2009, *A&A*, 501, 619
- Padovani, M., Hennebelle, P., Marcowith, A., & Ferrière, K. 2015, *A&A*, 582, L13
- Padovani, M., Ivlev, A. V., Galli, D., & Caselli, P. 2018, *A&A*, 614, A111
- Padovani, M., Ivlev, A. V., Galli, D., et al. 2020, *Space Sci. Rev.*, 216, 29
- Padovani, M., Marcowith, A., Hennebelle, P., & Ferrière, K. 2016, *A&A*, 590, A8
- Palmeirim, P., André, P., Kirk, J., et al. 2013, *A&A*, 550, A38
- Pety, J. 2005, in *SF2A-2005: Semaine de l'Astrophysique Française*, ed. F. Casoli, T. Contini, J. M. Hameury, & L. Pagani, 721
- Pineda, J. E., Arzoumanian, D., Andre, P., et al. 2023, in *Astronomical Society of the Pacific Conference Series*, Vol. 534, *Protostars and Planets VII*, ed. S. Inutsuka, Y. Aikawa, T. Muto, K. Tomida, & M. Tamura, 233
- Pineda, J. E., Sipilä, O., Segura-Cox, D. M., et al. 2024, *A&A*, 686, A162
- Pineda, J. L., Goldsmith, P. F., Chapman, N., et al. 2010, *ApJ*, 721, 686
- Punanova, A., Caselli, P., Pineda, J. E., et al. 2018, *A&A*, 617, A27
- Redaelli, E., Bizzocchi, L., Caselli, P., et al. 2018, *A&A*, 617, A7
- Redaelli, E., Bizzocchi, L., Caselli, P., et al. 2019, *A&A*, 629, A15
- Redaelli, E., Bovino, S., Giannetti, A., et al. 2021a, *A&A*, 650, A202
- Redaelli, E., Bovino, S., Lupi, A., et al. 2024, *A&A*, 685, A67
- Redaelli, E., Bovino, S., Sanhueza, P., et al. 2022, *ApJ*, 936, 169
- Redaelli, E., Sipilä, O., Padovani, M., et al. 2021b, *A&A*, 656, A109
- Redaelli, E., Spezzano, S., Caselli, P., et al. 2025, *arXiv e-prints*, arXiv:2502.13745
- Roy, A., André, P., Palmeirim, P., et al. 2014, *A&A*, 562, A138
- Sabatini, G., Bovino, S., Giannetti, A., et al. 2020, *A&A*, 644, A34
- Sabatini, G., Bovino, S., & Redaelli, E. 2023, *ApJ*, 947, L18
- Sabatini, G., Podio, L., Codella, C., et al. 2024, *A&A*, 684, L12
- Schuller, F., Urquhart, J. S., Csengeri, T., et al. 2021, *MNRAS*, 500, 3064
- Shu, F. H., Adams, F. C., & Lizano, S. 1987, *ARA&A*, 25, 23
- Sicilia-Aguilar, A., Henning, T., Linz, H., et al. 2013, *A&A*, 551, A34
- Sipilä, O., Caselli, P., & Harju, J. 2015, *A&A*, 578, A55
- Socci, A., Sabatini, G., Padovani, M., Bovino, S., & Hacar, A. 2024, *A&A*, 687, A70
- Sokolov, V., Wang, K., Pineda, J. E., et al. 2017, *A&A*, 606, A133
- Spezzano, S., Caselli, P., Bizzocchi, L., Giuliano, B. M., & Lattanzi, V. 2017, *A&A*, 606, A82
- Spezzano, S., Redaelli, E., Caselli, P., et al. 2025, *A&A*, 694, A27
- Spitzer, L. 1978, *Physical processes in the interstellar medium*
- Stone, E. C., Cummings, A. C., Heikkilä, B. C., & Lal, N. 2019, *Nature Astronomy*, 3, 1013
- Tiné, S., Roueff, E., Falgarone, E., Gerin, M., & Pineau des Forêts, G. 2000, *A&A*, 356, 1039
- van der Tak, F. F. S., Black, J. H., Schöier, F. L., Jansen, D. J., & van Dishoeck, E. F. 2007, *A&A*, 468, 627
- van Dishoeck, E. F. & Black, J. H. 1982, *ApJ*, 258, 533
- Vastel, C., Caselli, P., Ceccarelli, C., et al. 2006, *ApJ*, 645, 1198
- Wakelam, V., Herbst, E., Loison, J. C., et al. 2012, *ApJS*, 199, 21
- Wilson, T. L. 1999, *Reports on Progress in Physics*, 62, 143
- Wootten, A., Snell, R., & Glassgold, A. E. 1979, *ApJ*, 234, 876

## Appendix A: Spectral fit in the full sample

Figures A.1 to A.18 show the spectral fit performed with PYSPECKIT in each of the cores not shown in the Main Text. Table A.1 summarises the best-fit values obtained for the kinematic parameters ( $V_{\text{lsr}}$  and  $\sigma_V$ ), together with the peak optical depth of each transition. Figure A.19 shows the comparison of the centroid velocity and dispersion values for  $\text{H}^{13}\text{CO}^+$  and  $\text{DCO}^+$ .

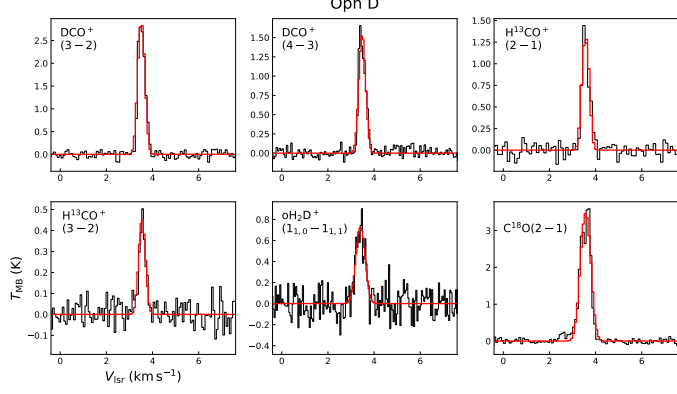


Fig. A.1.

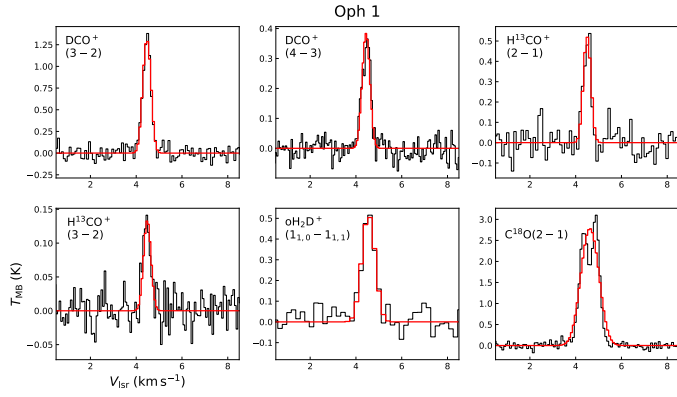


Fig. A.2. Same as Fig. A.1, but for Oph 1.

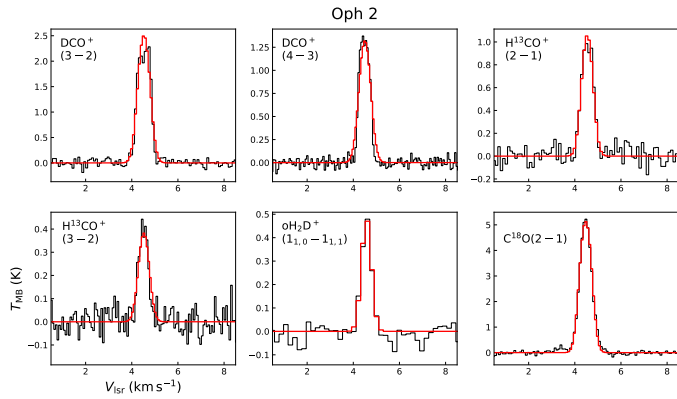


Fig. A.3. Same as Fig. A.1, but for Oph 2.

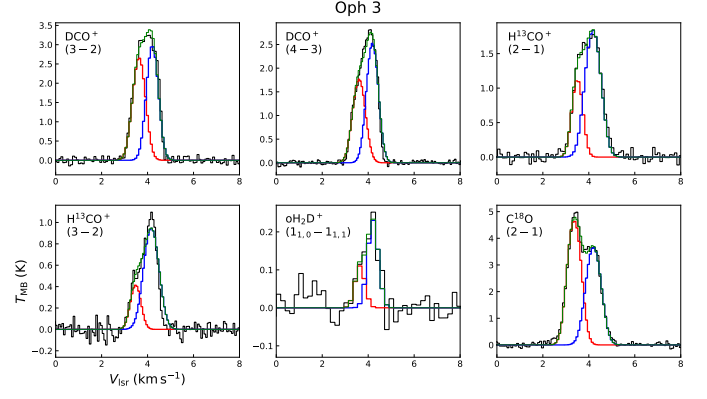


Fig. A.4. Same as Fig. A.1, but for Oph 3. As for Oph 4, we performed a two-velocity-component fit. The two distinct components are shown with the red and blue curves, whilst the green curve shows the total fit.

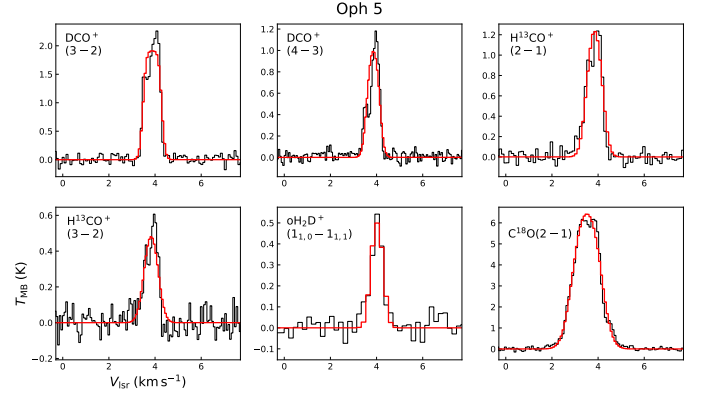


Fig. A.5. Same as Fig. A.1, but for Oph 5.

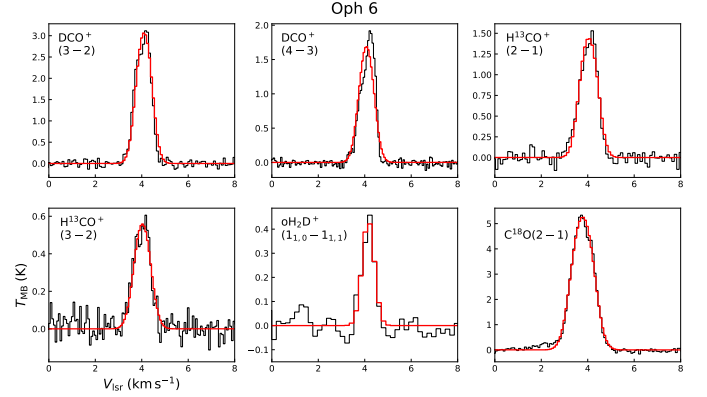
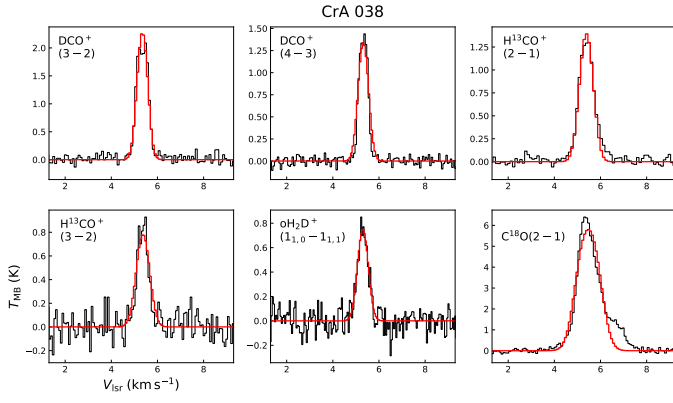
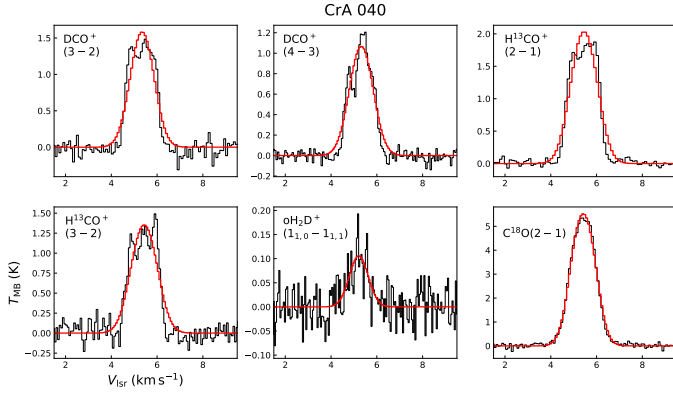


Fig. A.6. Same as Fig. A.1, but for Oph 6.





**Fig. A.7.** Same as Fig. A.1, but for CrA 038.



**Fig. A.8.** Same as Fig. A.1, but for CrA 040.

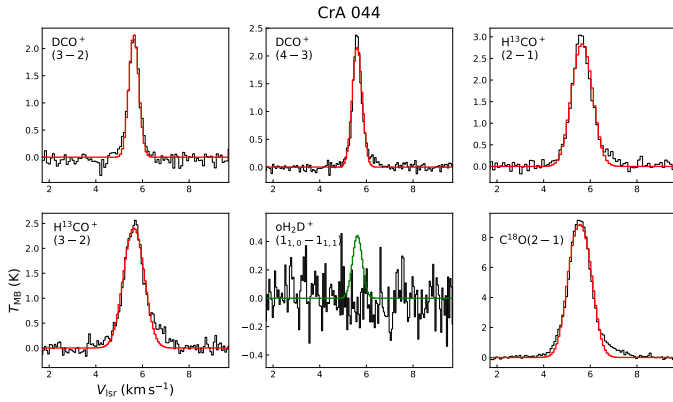


**Fig. A.9.** Same as Fig. A.1, but for CrA 044. In this case, the  $\text{oH}_2\text{D}^+(1_{1,0} - 1_{1,1})$  line is not detected given the sensitivity. The green curve shows the  $3\sigma$  upper limit obtained from the column density upper limit listed in Table 3, and the centroid velocity and linewidth of the  $\text{DCO}^+$  fit.

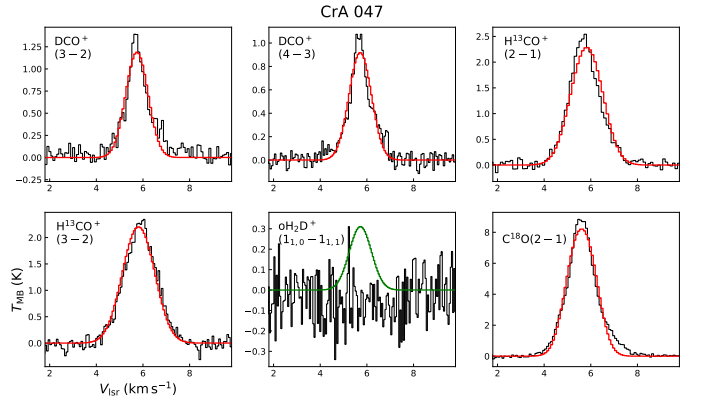


**Fig. A.10.** Same as Fig. A.1, but for CrA 047. In this case, the  $\text{oH}_2\text{D}^+(1_{1,0} - 1_{1,1})$  line is not detected given the sensitivity. The green curve shows the  $3\sigma$  upper limit obtained from the column density upper limit listed in Table 3, and the centroid velocity and velocity dispersion of the  $\text{DCO}^+$  fit.

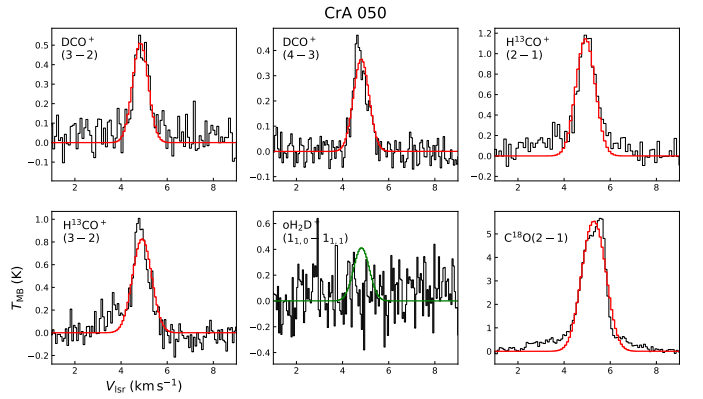


**Fig. A.11.** Same as Fig. A.1, but for CrA 050. In this case, the  $\text{oH}_2\text{D}^+(1_{1,0} - 1_{1,1})$  line is not detected given the sensitivity. The green curve shows the  $3\sigma$  upper limit obtained from the column density upper limit listed in Table 3, and the centroid velocity and velocity dispersion of the  $\text{DCO}^+$  fit.

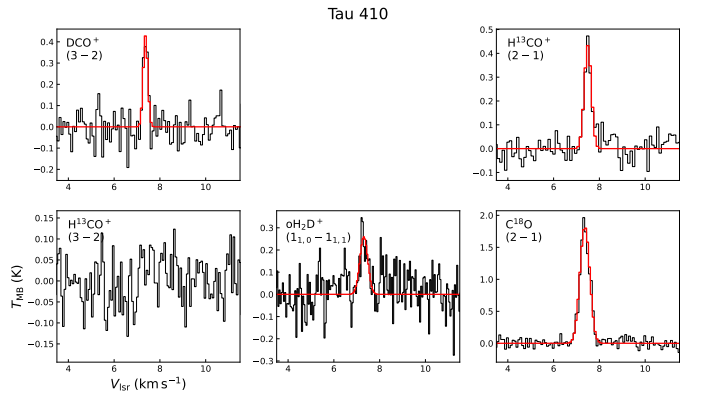


**Fig. A.12.** Same as Fig. A.1, but for Tau 410.

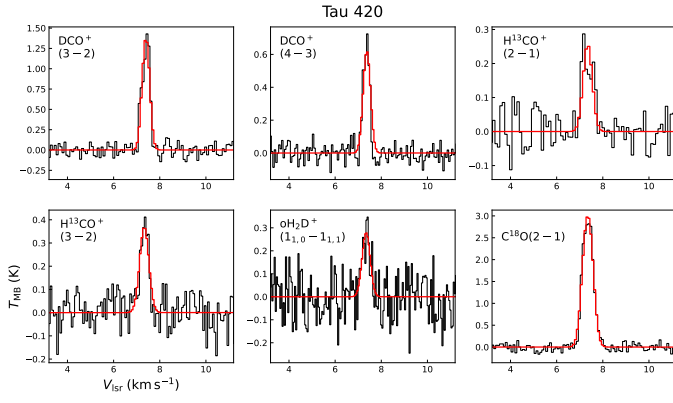


Fig. A.13. Same as Fig. A.1, but for Tau 420.

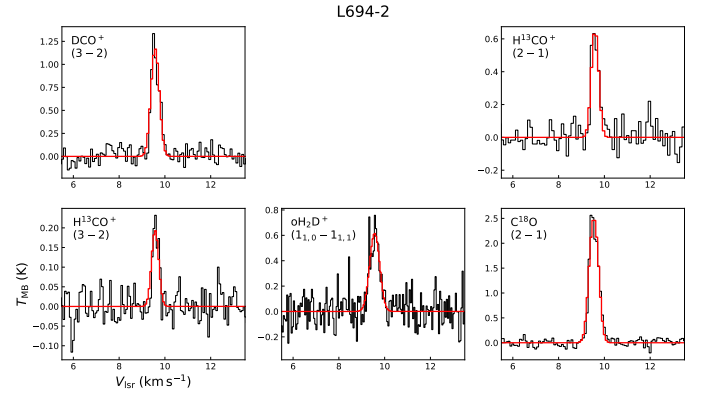


Fig. A.17. Same as Fig. A.1, but for L694-2.

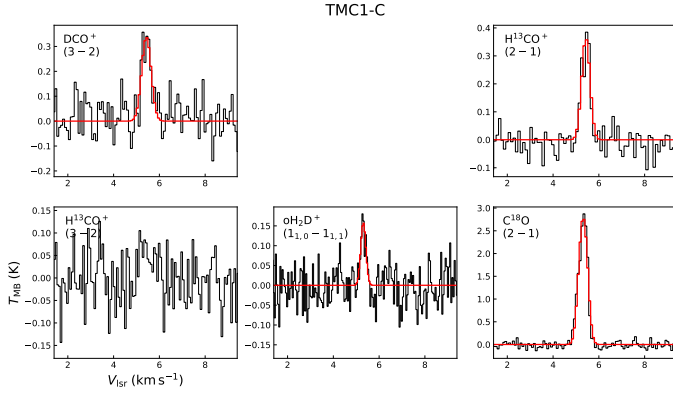


Fig. A.14. Same as Fig. A.1, but for TMC1-C.

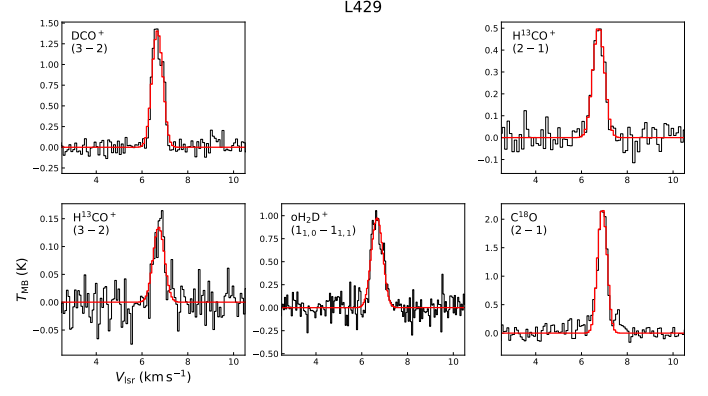


Fig. A.18. Same as Fig. A.1, but for L429.

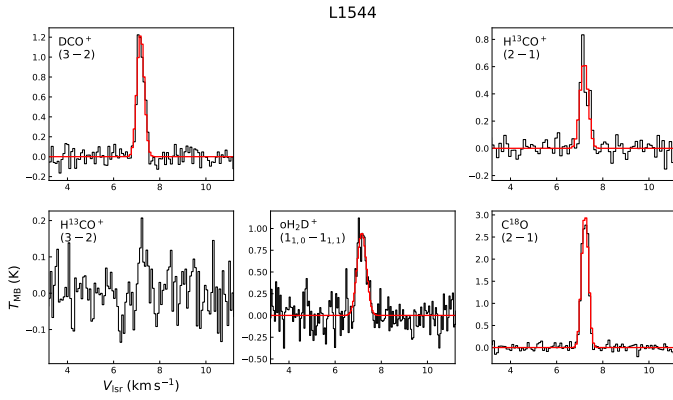


Fig. A.15. Same as Fig. A.1, but for L1544.

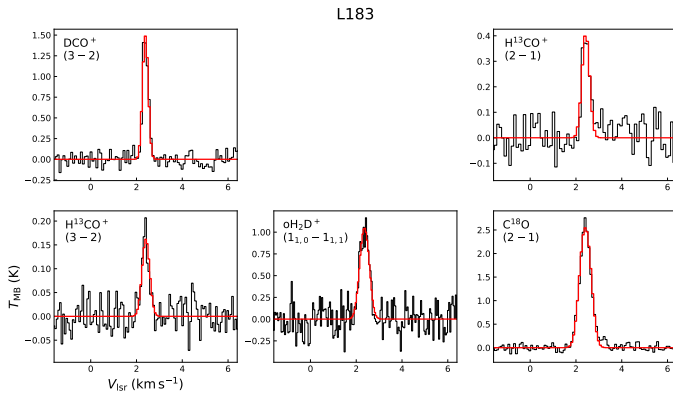
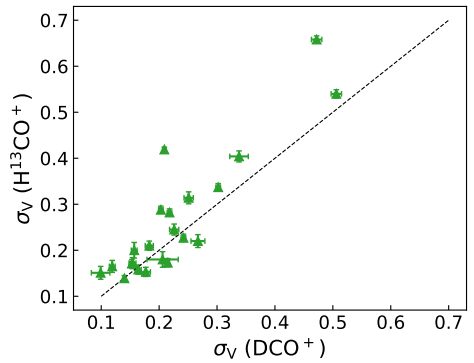
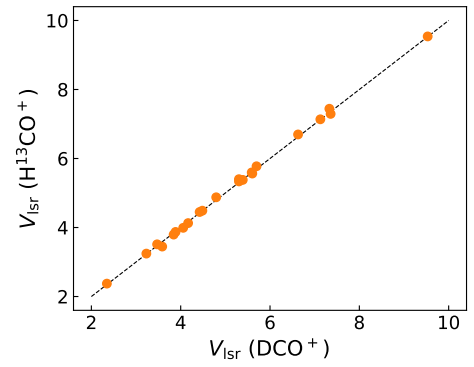


Fig. A.16. Same as Fig. A.1, but for L183.


 Fig. A.19. Comparison of the DCO<sup>+</sup> and H<sup>13</sup>CO<sup>+</sup> centroid velocities (top panel) and velocity dispersions (bottom panel). The dashed lines show the 1:1 relation.

**Table A.1.** The table summarises the best-fit values for the centroid velocity  $V_{\text{lsr}}$  and the velocity dispersion  $\sigma_V$  obtained with `pySPECKIT`, together with the estimated peak opacity of each transition.

Source	DCO <sup>+</sup>			H <sup>13</sup> CO <sup>+</sup>			oH <sub>2</sub> D <sup>+</sup>			C <sup>18</sup> O		
	$V_{\text{lsr}}$ km s <sup>-1</sup>	$\sigma_V$ km s <sup>-1</sup>	$\tau$	$V_{\text{lsr}}$ km s <sup>-1</sup>	$\sigma_V$ km s <sup>-1</sup>	$\tau$	$V_{\text{lsr}}$ km s <sup>-1</sup>	$\sigma_V$ km s <sup>-1</sup>	$\tau$	$V_{\text{lsr}}$ km s <sup>-1</sup>	$\sigma_V$ km s <sup>-1</sup>	$\tau$
Tau 410	7.329 ± 0.016	0.099 ± 0.016	0.07	7.442 ± 0.014	0.151 ± 0.014	0.12	-	-	-	7.317 ± 0.006	0.204 ± 0.005	0.31
Tau 420	7.357 ± 0.005	0.157 ± 0.005	0.32	7.293 ± 0.017	0.200 ± 0.017	0.01	0.02	0.17 ± 0.03	0.09	7.302 ± 0.004	0.215 ± 0.004	0.46
TMCI-C	5.39 ± 0.03	0.21 ± 0.03	0.06	5.380 ± 0.017	0.180 ± 0.017	0.10	-	0.11 ± 0.02	0.04	5.267 ± 0.004	0.180 ± 0.003	0.53
L1544	7.127 ± 0.007	0.154 ± 0.006	0.26	7.136 ± 0.012	0.172 ± 0.012	0.23	-	0.191 ± 0.017	0.34	7.182 ± 0.003	0.135 ± 0.002	0.74
L183	2.347 ± 0.005	0.119 ± 0.005	0.39	2.374 ± 0.013	0.165 ± 0.013	0.14	0.08	0.193 ± 0.014	0.45	2.363 ± 0.004	0.227 ± 0.003	0.69
L429	6.628 ± 0.009	0.226 ± 0.008	0.34	6.697 ± 0.012	0.245 ± 0.012	0.32	0.12	0.236 ± 0.012	0.39	6.864 ± 0.006	0.192 ± 0.005	0.52
L694-2	9.530 ± 0.008	0.177 ± 0.008	0.28	9.538 ± 0.011	0.153 ± 0.010	0.38	0.15	0.211 ± 0.019	0.23	9.493 ± 0.004	0.187 ± 0.004	0.63
Oph 1	4.424 ± 0.005	0.164 ± 0.005	0.71	4.450 ± 0.010	0.158 ± 0.010	0.36	0.12	0.27 ± 0.02	0.49	4.575 ± 0.009	0.370 ± 0.008	0.39
Oph 2	4.485 ± 0.004	0.242 ± 0.004	0.59	4.488 ± 0.008	0.227 ± 0.008	0.58	0.26	0.213 ± 0.018	0.14	4.425 ± 0.002	0.229 ± 0.002	0.93
Oph 3-1 <sup>a</sup>	3.59 ± 0.02	0.267 ± 0.012	0.38	3.45 ± 0.02	0.220 ± 0.014	0.60	0.28	0.22 ± 0.13	0.02	3.318 ± 0.009	0.269 ± 0.005	0.91
Oph 3-2 <sup>a</sup>	4.166 ± 0.016	0.251 ± 0.008	0.25	4.13 ± 0.02	0.314 ± 0.013	0.69	0.41	0.23 ± 0.07	0.02	4.155 ± 0.012	0.306 ± 0.009	0.64
Oph 4-1 <sup>a</sup>	3.231 ± 0.007	0.183 ± 0.007	0.80	3.244 ± 0.010	0.210 ± 0.010	0.75	0.34	0.28 ± 0.15	0.15	2.966 ± 0.012	0.257 ± 0.004	0.66
Oph 4-2 <sup>a</sup>	3.885 ± 0.003	0.153 ± 0.004	0.64	3.872 ± 0.010	0.171 ± 0.009	0.60	0.28	0.19 ± 0.03	0.18	3.68 ± 0.02	0.391 ± 0.011	0.93
Oph 5	3.842 ± 0.005	0.203 ± 0.004	5.01	3.795 ± 0.008	0.288 ± 0.008	0.65	0.30	0.229 ± 0.018	0.83	3.468 ± 0.004	0.467 ± 0.004	1.22
Oph 6	4.056 ± 0.004	0.302 ± 0.004	0.77	3.991 ± 0.007	0.337 ± 0.008	0.93	0.41	0.26 ± 0.02	0.12	3.736 ± 0.003	0.417 ± 0.003	0.88
Oph D	3.472 ± 0.002	0.140 ± 0.002	0.75	3.513 ± 0.005	0.139 ± 0.006	1.03	0.41	0.191 ± 0.017	0.23	3.520 ± 0.004	0.210 ± 0.004	0.53
CrA 038	5.305 ± 0.004	0.218 ± 0.004	0.39	5.336 ± 0.009	0.282 ± 0.008	0.38	0.26	0.227 ± 0.013	0.17	5.425 ± 0.008	0.429 ± 0.007	1.06
CrA 040	5.304 ± 0.009	0.506 ± 0.009	0.19	5.401 ± 0.010	0.540 ± 0.009	0.45	0.36	0.41 ± 0.05	0.02	5.370 ± 0.003	0.478 ± 0.003	0.73
CrA 044	5.590 ± 0.003	0.209 ± 0.003	0.14	5.596 ± 0.005	0.419 ± 0.005	0.42	0.42	-	-	5.505 ± 0.004	0.422 ± 0.003	1.10
CrA 047	5.698 ± 0.009	0.472 ± 0.009	0.11	5.775 ± 0.008	0.658 ± 0.008	0.25	0.28	-	-	5.562 ± 0.006	0.548 ± 0.005	0.89
CrA 050	4.795 ± 0.016	0.338 ± 0.016	0.05	4.876 ± 0.013	0.404 ± 0.012	0.19	0.17	-	-	5.241 ± 0.007	0.476 ± 0.007	0.56
CrA 151	5.603 ± 0.004	0.215 ± 0.003	0.34	5.564 ± 0.009	0.173 ± 0.009	0.54	0.26	0.20 ± 0.03	0.14	5.456 ± 0.006	0.298 ± 0.005	0.67

**Notes.** <sup>(a)</sup> For Oph 3 and Oph 4 we report the fit values of both velocity components.

## Appendix B: LVG modelling of the $\text{H}^{13}\text{CO}^+$ lines

Given the availability of multiple transitions of  $\text{H}^{13}\text{CO}^+$  for almost all the targets, we have used these data to perform simple LVG (large-velocity-gradient) calculation using the RADEX software (van der Tak et al. 2007; Dwiriyanti et al., *subm.*). This allows us to *i*) infer  $n(\text{H}_2)$  independently from the *Herschel* data; *ii*) re-evaluate the path length  $L = N(\text{H}_2)/n(\text{H}_2)$ ; and *iii*) confirm the sub-thermal excitation for this species. We have used RADEX to compute escape probabilities, adopting the LVG approach. The LAMDA (Leiden Atomic and Molecular Database) file for  $\text{H}^{13}\text{CO}^+$  has been taken from the EMAA database<sup>8</sup>. We consider para- $\text{H}_2$  the main collisional partner. For the sake of simplicity, we have excluded from this analysis the two sources with clear multiple velocity components in all lines (Oph 3 and Oph 4), and the 3 sources with only upper limits for the  $\text{H}^{13}\text{CO}^+$  (3-2) transition (Tau 410, TMC1-C, L1544). The number of analysed targets is 15.

We proceeded to input into the RADEX calculation the  $\text{H}^{13}\text{CO}^+$  column density and the line width (FWHM) derived in Sect. 4.2. We used the dust temperatures in Table 1 as a proxy for the gas temperature, and the gas volume densities obtained from the  $N(\text{H}_2)$  values (Table 1, assuming  $L = 0.1$  pc). We refer to this quantity as  $n(\text{H}_2)_{\text{cont}}$ , as it is derived from the *Herschel* continuum data.

We checked the results, comparing the modelled line intensities with the observed ones. Table B.1 reports the  $n(\text{H}_2)_{\text{cont}}$  values for each source, together with the lines peak intensity, both observed and modelled by RADEX. We also list the ratio  $T_{\text{peak}}^{\text{mod}}/T_{\text{peak}}^{\text{obs}}$ . These results show that for 14 out of 15 targets, the (2-1) line intensity is reproduced within a factor of 2, and for the (3-2) lines, this holds for 6 targets. Since the (3-2) line has a better angular resolution and higher critical density, this suggests that the  $n(\text{H}_2)_{\text{cont}}$  values underestimate the central volume density. This is expected due to the fact that this quantity is computed from the *Herschel* low-resolution data, and it represents an average along the line-of-sight and on the beam. Figure B.1 shows the RADEX results concerning the (3-2) to (2-1) line intensity ratio for a grid of gas temperature and  $n(\text{H}_2)$  values. We overplot the curves corresponding to the observed cores. The plot shows that the  $\text{H}^{13}\text{CO}^+$  observations are consistent with volume density values from several  $\times 10^4 \text{ cm}^{-3}$  to  $10^6 \text{ cm}^{-3}$ , given the typical cores' temperatures of 10 – 20 K.

In order to quantify the underestimation, we have increased  $n(\text{H}_2)$  and we ran the LVG computation again. First, we input  $n(\text{H}_2) = 2 \times n(\text{H}_2)_{\text{cont}}$ . This is sufficient to reproduce the line intensities within a factor of 2 in all sources except two. The only targets where the emission is still underestimated are L183 (10% for the 2-1, 60% for the 3-2), for which a correction  $n(\text{H}_2) = 3 \times n(\text{H}_2)_{\text{cont}}$  is needed, and Tau 420, which is a peculiar source due to the fact that the (3-2) line is brighter than the (2-1) (this is also the only source where we see suprathermal excitation in  $\text{H}^{13}\text{CO}^+$ , see Table 3 and Fig. A.19). We can conclude that the  $n(\text{H}_2)_{\text{cont}}$  volume densities are underestimated by a factor of  $\sim 2$ .

We have re-computed the  $\zeta_2$  values assuming  $L = 0.05$  pc for those 9 sources that needs the correction. The results are shown in Fig B.2, as a function of the dust temperature. We still detect the increase of  $\zeta_2$  with increasing  $T_{\text{dust}}$ . The black curve shows the linear best fit to the data. The trend is shallower and the uncertainties are higher (due to the reduced statistics), but our results still hold. We highlight that the LVG methodology entrails

a number of uncertainties, the main ones being *i*) the  $T_{\text{gas}} = T_{\text{dust}}$  assumption; *ii*) the source geometry, which is ignored.

The RADEX analysis confirms that the  $\text{H}^{13}\text{CO}^+$  transition are subthermally excited. The  $\tau$  values computed by RADEX are in general in good agreement with those listed in Table A.1, confirming that the lines are optically thin.

**Table B.1.** Results of the RADEX analysis. For each source, we report the  $\text{H}_2$  volume density estimated from *Herschel*, the modelled vs observed peak temperature of the  $\text{H}^{13}\text{CO}^+$  lines, and their ratio  $T_{\text{peak}}^{\text{mod}}/T_{\text{peak}}^{\text{obs}}$ .

Source	$n(\text{H}_2)_{\text{cont}}$ $10^5 \text{ cm}^{-3}$	$T_{\text{peak}}^{\text{obs}}$ K	(2-1) $T_{\text{peak}}^{\text{mod}}$ K	ratio	$T_{\text{peak}}^{\text{obs}}$ K	(3-2) $T_{\text{peak}}^{\text{mod}}$ K	ratio
Tau 420	1.3	0.3	0.1	0.4	0.4	0.03	0.1
L183	1.9	0.4	0.2	0.6	0.2	0.04	0.2
L429	1.7	0.5	0.4	0.8	0.2	0.1	0.5
L694-2	1.4	0.6	0.4	0.7	0.2	0.1	0.3
Oph 1	1.2	0.5	0.5	0.9	0.1	0.1	0.8
Oph 2	1.7	1.0	1.0	1.1	0.4	0.3	0.6
Oph 5	1.7	1.2	1.2	1.0	0.6	0.3	0.6
Oph 6	1.5	1.5	1.5	1.0	0.6	0.4	0.7
Oph D	0.5	1.4	0.8	0.6	0.5	0.2	0.3
CrA 038	2.0	1.3	1.0	0.8	0.9	0.3	0.3
CrA 040	1.5	1.9	1.2	0.7	1.5	0.4	0.3
CrA 044	3.4	3.0	2.6	0.8	2.6	1.2	0.5
CrA 047	3.2	2.5	1.9	0.8	2.3	0.9	0.4
CrA 050	1.1	1.2	0.6	0.5	1.0	0.2	0.2
CrA 151	1.3	1.2	0.7	0.6	0.5	0.2	0.3

<sup>8</sup> <https://emaa.osug.fr>.

(3-2)/(2-1)

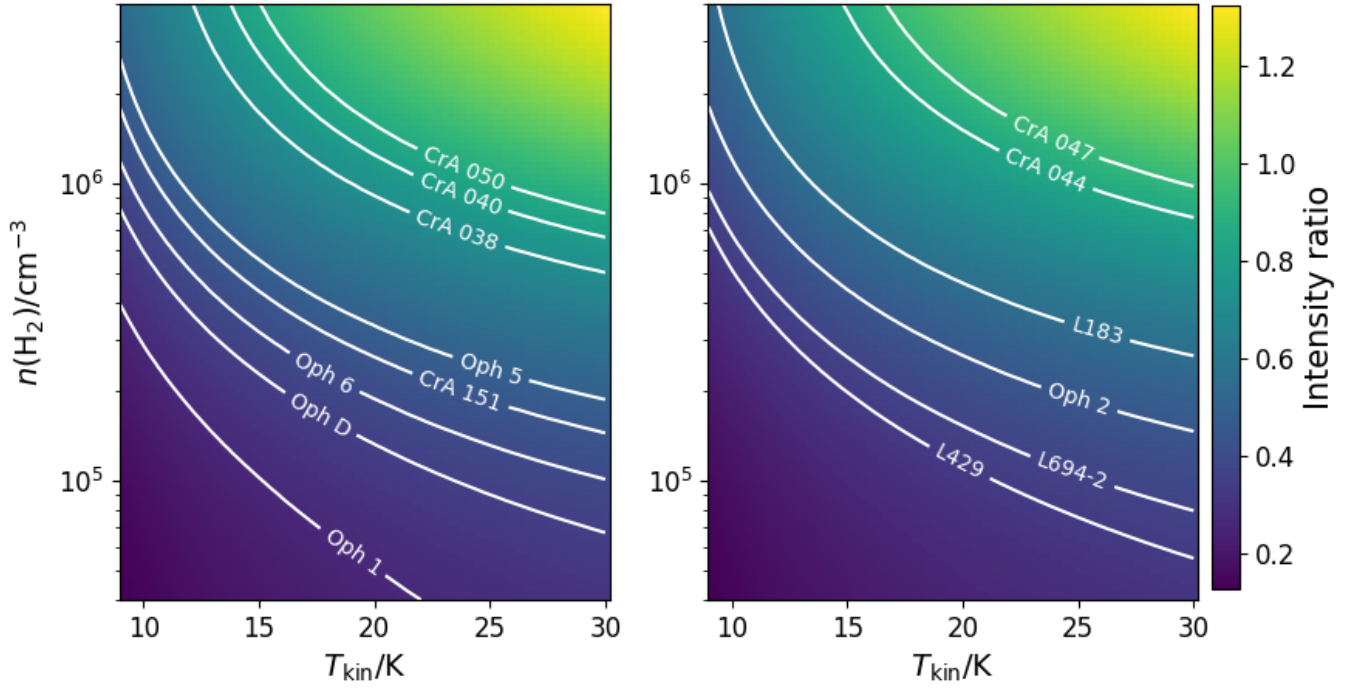


**Fig. B.1.**  $\text{H}^{13}\text{CO}^+$  line intensity ratio (3-2)/(2-1) as a function of  $\text{H}_2$  volume density versus gas kinetic temperature ( $T_{\text{kin}}$ ). The plot has been obtained with RADEX, assuming the average  $\text{H}^{13}\text{CO}^+$  column density measured in the sample ( $9.4 \times 10^{11} \text{ cm}^{-2}$ ). The curves, labelled by object, show the observed values.

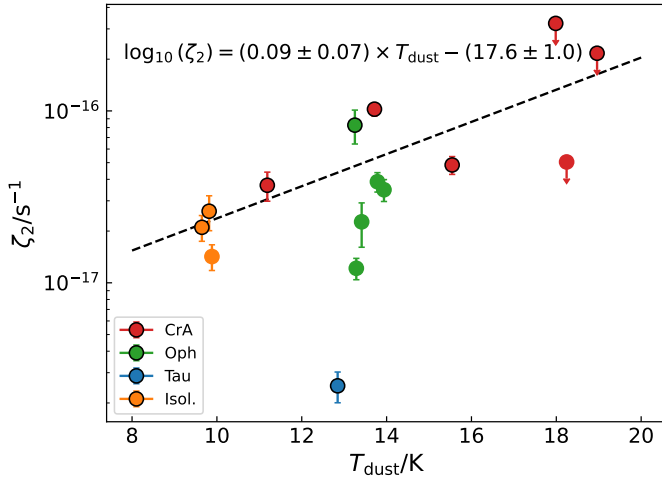


**Fig. B.2.** Plot of  $\zeta_2$  as a function of  $T_{\text{dust}}$ , where the  $n(\text{H}_2)$  values have been re-evaluated from the  $\text{H}^{13}\text{CO}^+$  line emission, as explained in the Text. The sources where we increased  $n(\text{H}_2)_{\text{cont}}$  in the LVG calculations are shown with black edges. The dashed black curve shows the linear best fit to the data, in log-linear space.